Textile-Based Electromagnetic Soft Strain Sensors for Fast Frequency Movement and their Application in Wearable Devices Measuring Multi-Axial Hip Joint Angles during Running

by

Mohammad Tavassolian

B.A.Sc., Tallinn University of Technology, 2017

Thesis Submitted in Partial Fulfillment of the
Requirements for the Degree of
Master of Applied Sciences

in the
School of Mechatronics Systems Engineering
Faculty of Applied Sciences

SIMON FRASER UNIVERSITY

Spring 2020

Approval

Name:	**Mohammad Tavassolian**
Degree:	**Master of Applied Science**
Title:	**Textile-based Inductive Soft Strain Sensors for Fast Frequency Movement and their Application in Wearable Devices Measuring Multi-Axial Hip Joint Angles during Running**
Examining Committee:	**Chair:** Helen Bailey Lecturer
	Carlo Menon Senior Supervisor Professor
	Behraad Bahreyni Supervisor Associate Professor
	Amr Marzouk Internal Examiner Lecturer
Date Defended/Approved:	March 05, 2020

Ethics Statement

The author, whose name appears on the title page of this work, has obtained, for the research described in this work, either:

a. human research ethics approval from the Simon Fraser University Office of Research Ethics

or

b. advance approval of the animal care protocol from the University Animal Care Committee of Simon Fraser University

or has conducted the research

c. as a co-investigator, collaborator, or research assistant in a research project approved in advance.

A copy of the approval letter has been filed with the Theses Office of the University Library at the time of submission of this thesis or project.

The original application for approval and letter of approval are filed with the relevant offices. Inquiries may be directed to those authorities.

Simon Fraser University Library
Burnaby, British Columbia, Canada

Update Spring 2016

Abstract

Wearable in situ multi-axis motion tracking with inductive sensors and machine learning is presented. The production, characterization, and use of a modular and size adjustable inductive sensor for kinematic motion tracking are introduced. The sensor was highly stable and able to track high frequency (>15Hz) and high strain rates (>450%/s). Four sensors were used to fabricate a pair of motion capture shorts. A random forest machine learning algorithm was used to predict the sagittal, transverse, and frontal hip joint angle using the raw signals from the sport shorts strain sensors during running with a cohort of 12 participants against a gold standard optical motion capture system to an accuracy as high as $R^2 = 0.98$ and an RMSE of 2° in all three planes. This present study provides an alternative strain sensor to those typically used (piezoresistive/capacitive) for soft wearable motion capture devices with distinct advantages that could find applications in smart wearable devices, robotics, or direct integration into textiles.

Keywords: inductive sensors, kinematic tracking, soft sensors, smart sensors, wearable device

Acknowledgements

I would like to thank my senior supervisor, Dr. Carlo Menon, for his unconditional support and guidance. Additionally, I would like to thank everyone in MENRVA research group for being such amazing group of colleagues that I had chance to work with.

My sincere appreciation goes to my family, Hatef, Nahid and Hamed for supporting me throughout these years.

Table of Contents

List of Tables

List of Figures

List of Acronyms

CCET	Copper-coiled elastic thread
EMS	Electromagnetic measurement systems
IMS	Image processing systems
MSE	Mean squared error
NRMSE	Normalized root mean squared error
OMC	Optoelectric motion capture systems
PBK	Peak braking force
PCB	Printed circuit board
RE	Running economy
RMSE	Root mean squared error

Chapter 1.

Introduction

1.1. Background

Demands and benefits in monitoring human-body extremities have been increasing in recent years. Running has been one of the most popular physical activity among individuals [1], [2]. This growth might explain the increased scientific interest in studying performance characteristics of recreational and master athletes [3]. With the growth of the population of runners, there has also been a significant increase in reports related to preventable running-associated injuries [4], [5]. There have been studies showing that running performance can be enhanced using specific running techniques related to lower body kinematics[6]. Optical motion capture systems (OMCs) can monitor human body kinematics in lab environments but are not suitable for outdoors and in larger areas. This could be the potential room where wearable technologies can be developed and utilized to monitor lower body extremities not only in lab environments but also outdoors.

Sport-related injuries could be highly associated with kinetic as well as kinematic variables during running. Kinetic variables such as peak braking force (PBK) were found to be related to a significantly larger injury hazard ratio among female recreational runners and need to be reconsidered for gait retraining interventions [5]. In another study, a major reduction of PBK variable was obtained by a combination of an increase in the step frequency and a decrease in the step length. A technology sufficiently lightweight and affordable can be developed that could provide all or part of the biofeedback needed, usable through everyday activities such as outdoor running.

Running induced fatigue, as an essential component, can have considerable and observable effects on three-dimensional lower extremity joint movements. A study was carried out that targeted monitoring the changes in non-sagittal lower body joint angle kinematics during a 10 km treadmill run with near-maximum effort [6]. Comparing the final 10 km with the initial 0 km measurement, peak deviation of 3°, 3.5° and 5° for the hip (more abduction) and knee (more abduction) and ankle (more eversion) were observed.

It was concluded that running with a more abducted knee joint and with higher demand for hip abductor muscles in the unfatigued state was correlated to more significant fatigue-inducted changes of joint kinematics at the two joints [6].

Wearable electronics have been increasing in popularity—including both commercial products and peer-reviewed reports—as the advancement of materials, electronics, and printed circuit boards (PCBs) allows a decrease in size, seamless integration, and improvements in performance [8]. Wearable electronics can provide useful of data such as, but not limited to, pressure [9], biosignal [10], biochemical [11], and strain [12] [13] that can be used to provide users with a variety of metrics. Textile based sensors have been developed to track strain [13], [14] and pressure [9]. Electromagnetic tracking [15] and optoelectric motion capture (OMC) systems [16] are capable of providing accurate kinematic human motion data, which may be used to prevent injury [7] and enhance performance [17]. OMC systems are only able to provide accurate information under certain conditions—typically limited to specific spaces and line-of-sight requirements. Factors such as marker influence on user movement, requirement for expensive, sophisticated hardware, precise marker placement, and marker movement during use can decrease the accuracy of the OMCs [18]–[20]. The spatial limitation of motion tracking systems reduces the ability to use these systems to track everyday activities where they could be highly useful for sports, rehabilitation, and occupational settings. Two alternatives include inertial measurement units (IMUs) and flexible strain sensors (i.e. resistive, capacitive, and inductive), both of which are not spatially limited.

1.2. Motivation and objective

Inductive-based strain sensors have also been used to estimate [21], [22] and classify [23] human body motion in one plane, however, there have not been numerous works to monitor the human body motion in multi-axis using these sensors. Inductive sensors offer their overtime signal stability and configurable sensitivity, which can potentially be highly preferred over other wearable motion capture systems. This thesis aims to develop an inductive-based strain sensor, using low-cost available materials requiring no chemical processes which offer reproducibility. The performance of the fabricated sensor under various active and passive tensile tests is to be studied. Finally, a commercially available sports garment is equipped with four inductive sensors to track

hip joint angle during running using a machine learning technique. As a result, the objectives of this thesis are listed as follows:

1. Fabrication of a soft spring-inspired inductive-based soft strain sensor requiring inexpensive materials.

2. Characterization of the strain sensor for generic strain monitoring tests.

3. Preparation and evaluation of a pair of smart sports shorts for monitoring hip joint angle in 3-dimensions using only four strain sensors.

1.3. Scientific Contributions

The results of this research led to the following academic journal publication and provisional patent:

- M. Tavassolian, Dr. T. Cuthbert, Dr. C. Napier, Dr. J. Peng, Prof. C. Menon, “Textile-Based Inductive Soft Strain Sensors for Fast Frequency Movement and their Application in Wearable Devices Measuring Multiaxial Hip Joint Angles During Running”, Advanced Intelligent Systems. DOI: 10.1002/aisy.201900165

- C. Menon, M. Tavassolian, A.G. Patiño, “Measurement Apparatus and Method For Monitoring Physiological Signs“

1.4. Thesis outline

Chapter 2. In this chapter, a literature review was conducted on in-lab motion capturing systems as well as alternative wearable devices. Advantages and shortcomings of optical and electromagnetic motion capturing systems as well as wearable alternatives such as IMU and textile based were described based on some previous works available in literature.

Chapter 3. This chapter includes a literature review conducted over different strain-based wearable sensors based on their nature of operation (resistive, capacitive and inductive) and includes previous works attempted for tracking human body kinematics using resistive and capacitive strain sensors. This chapter is concluded by mentioning important requirements for strain sensors.

Chapter 4. This chapter provides information about fabrication process of the proposed inductive sensor which required an in-house built spur machine and cheap available materials avoiding any chemical procedures. The sensor's principle of operation was explained and two mathematical formulae for calculating sensor's signal were derived. Finally, a comprehensive set of tensile tests were conducted on the fabricated inductive sensor illustrating a thorough insight about various aspects of the sensor's performance.

Chapter 5. In this chapter, a smart sport compression shorts were prepared using the fabricated inductive sensor to measure hip joint angle. The reference hip joint angle measurement and the machine learning technique used for mapping sensor's raw data to hip joint angle were explained. Finally, the performance of the smart prototype was evaluated by running a cohort test among 12 healthy participants whose hip joint angle were measured and used for evaluation of the wearable system.

Chapter 6. This chapter concludes the thesis by discussing how the objectives of this research work were achieved.

Chapter 2.

Literature review

2.1. In-lab motion capturing systems

Optical motion capturing systems can track the position of reflective markers in a limited space with less than one-millimetre accuracy (number of cameras, size of markers, etc. affect the accuracy). With the option of using reflective makers of variable size for different purposes, it is possible to measure and track human kinematics with high accuracy [24]. Given the sufficient accuracy and precision of such systems, they are often used as ‘ground truth’ source of data in the? kinetic and kinematic analysis [16]. However, there are factors associated with limitations of such systems to be used in everyday activities, such as spatial limitations, sensitive marker placement procedures and price.

By placing makers on studied anatomical landmarks, it is possible to construct a 3D model of different body segments, such as pelvis, shank, spine, etc. and track kinetic and kinematics variables during different activities. In a study, by placing reflective markers on 22 participants running on a 25 m runway at a speed of 3.5 m/s, it was possible to analyze their kinematic variables and the gender differences between male and female participants [25]. Although sufficiently accurate and valuable can be extracted from such systems that could lead to a lower risk of injury during running, they cannot be used by individuals, due to affordability as well as spatial limitations. For instance, multiple Infrared cameras have to be placed at fixed and stationary locations to track the reflective markers aside from the high cost of the motion capture systems, which are complex to use and need training sessions in advance.

Electromagnetic measurement systems (EMS) detect the unknown positions of the measurement transponders, using the time-of-flight of electromagnetic waves [26]. Despite offering a larger capture volume, EMS provides less accurate measurement and tracking compared to image processing systems (IMS) [26]. They do not require line-of-sight for measuring the position of transponders. However, their size of components needed during the measurements aside from electromagnetic noises and disturbances that might exist in the operating environment makes them inconvenient to be used in everyday activity as well as during athlete training or sports sessions.

Image processing systems (IMS) are generally more accurate than EMS, as well as offering a larger capture volume compared to OMC [26]. In IMS, RGB cameras are used to detect markers position in a 2D array of pixels, while in OMC, infrared cameras are used to detect the position of reflective markers in 3D. Using extensive software analysis, each frame of video captured are analyzed in order to obtain positions of parts of interest. This marker-less tracking systems can be used to detect events [27]. Using a Kinect camera, a 3D model of the human body was constructed, requiring no markers while using open-source software [28]. Image processing has some drawbacks as well, such as extensive computational resources demanded by the software which might not allow real-time operation in addition to the effect of number of cameras on the accuracy achieved [26], [29]. The most crucial limitation this system offers is the immobility of the cameras, i.e. in addition to costly computational resources required, cameras must be kept in place.

2.2. Wearable systems

2.2.1. IMU-based motion capturing systems

Inertial measurement units (IMUs) have been used frequently to provide orientation, angular velocity, and acceleration data in different axes with gyroscopes, magnetometers and accelerometers, respectively. IMU's have been used previously to measure lower extremities gait parameters [30]. However, significant performance limitations have been reported when using IMUs during long, fast, and complicated movements [30]. Additionally, the estimation of IMU orientation using magnetometers is affected by ferromagnetic disturbances that can lead to a reduced accuracy in measurements [31], [32].

It is possible to use only IMUs using sensor fusions algorithms such as Extended Kalman Filter to monitor and track lower body joint movements. In a study, multiple IMUs were used to measure movements of joints such as hip, knee and ankle of twenty-eight healthy participants when performing bilateral squats, single-leg squats and countermovement jumps [33]. It was possible to obtain an accuracy of below 3° compared to OMC measurements. In order to exclude the possible errors in the IMU-driven data based on different coordinates systems as well as the calibration process, the biomechanical model [34] and IMU-to-segment calibrations were calculated using OMC

data [33], [35]. In other words, in order to achieve a higher accuracy of measurement, OMC data was required for each participant. Additionally, the initialization of IMU-based kinematics estimation required OMC system's data [33].

In another study, full-body motion analysis was conducted comparing an IMU-based system and an OMC system which aimed to determine the technological error, biomechanical model differences between the two systems as well as evaluating the effect of task complexity and duration on the accuracy obtained [30]. Although this study concluded that the duration and complexity of a task affect the accuracy comparing the IMU-based system with an OMC system to some extend (no more than 2°), the definition of local coordinate systems, comparing the two systems, was found to be the most influential [30] [36].

Although IMUs are highly portable devices, compared to OMC, EMC and IMC, they might not be suitable for in situ kinematics monitoring in ergonomics [30] as well as sports applications due to their analysis error and their signal drift. Bias instability noise—as one type of technological error associated with gyroscopes—becomes a dominant orientation error component after less than ten seconds of integration time [37].

Gyroscopes—sensitive to vibration shocks [38] , which typically occur when feet hit the ground—can affect the accuracy of certain joints [30]. Additionally, due to fixation to the surface of the skin, the IMU signal might be subject to soft tissue artifact [20], which would affect the validity of the measurement of the underlying bones and joints. Given the mentioned limitations and other reported works [36], [39], joint angles measured by IMUs and an OMC were reported to be poorly correlated for the hip frontal plane [39].

2.2.2. Textile-based motion capturing systems

Flexible strain sensors are a possible alternative solution for human motion monitoring, which has been conducted and investigated for lower body monitoring [40]–[42] as well as upper body [43], [44]. When wearing tight-fitting garments, it is possible to associate the strain applied to the garment during some activity with one or more joint angles. This correlation can be used to output joint angles in at least one dimension, and the accuracy, durability and repeatability of such systems can be profoundly affected by the type and the number of strain sensors used.

In a study using OMC, strain values and patterns were obtained on a full-body stretchable cat-suit, targeting to classify upper body postures [44]. After determining the number and location of to-be-placed resistive strain sensors, it was possible to classify body posture out of a total of 27 complex classes, using a total of 21 resistive-based strain sensors. After obtaining a high classification accuracy of 0.97, it was shown that complex strain patterns could be associated with motion and posture [45].

In a detailed study, a total of 18 resistive-based sensors were incorporated in a sleeveless shirt to estimate tri-axial trunk motion angles during complex movements [43]. In this study, angle estimation in three planes was found to be below 4.26°. Although it was shown that the results obtained demonstrated the feasibility of using smart textiles to capture complicated movements, but it is essential to investigate if it is possible to build a system using similar sensors that are capable of accurate estimation of movements using a smaller number of sensors significantly.

A cohort investigation was carried out to estimate lower body joint movements in all planes using resistive sensors, achieving an accuracy of less 2.2° (RMSE), during five different speeds of running [46]. Resistive sensors can experience signal drift [43], [47], [48], which might not allow them to be used for long-term applications, which will be discussed in more detail in the next chapter.

Chapter 3.

Wearable strain sensors background

3.1. Wearable strain sensors

Wearable strain sensors are popular for monitoring human motions in daily activities as well as in sport due to comfortability and stretchability [49]. Following are the three types of strain sensors studied so far:

3.1.1. Resistive-based strain sensors

Piezoresistive strain sensors—these can be comprised of composites combining thermoplastic elastomers or elastic thermosets and conductive materials such as carbon nanotubes [50], polymers [51] and ionic liquids [52]—are relatively common and the most straightforward systems for signal analysis (voltage reading). Upon applying strain (changing the sensor's length), the resistivity of the sensor changes, and by placing the sensor in a simple voltage reading circuit, the sensor's signal can be obtained. Despite their low cost of production, low power consumption and non-sophisticated signal processing, most of the piezoresistive sensors rely on a mechanism of sensing, which is destructive. The piezoresistive mechanism—disconnection-reconnection of conductive pathways within the composite or the formation of cracks—are susceptible to irreversible signal drift and non-linear response to strain [49].

3.1.2. Capacitive-based strain sensors

Capacitive sensors are less common, more complex to fabricate, and require more advanced signal conditioning [53], [54] , but are advantageous since they rely on geometric changes to modulate the capacitance signal. Piezoresistive and capacitive sensors have been produced in both patch and fibre morphologies, increasing the ability to incorporate them seamlessly into textiles and garments. Capacitive sensors do not rely on a piezoresistance (although this can affect the resulting signal [53]), but a change in geometry. Capacitive sensors require specialized methods and materials for fabrication that may not result in scalability [55]. The advancement of piezoresistive and capacitive

sensors have included specialized manufacturing techniques, high-performance (and costly) conductive materials and unique layered architectures.

3.1.3. Inductive-based strain sensors

Inductive-based strain sensors commonly consist of a conductive material forming at least one loop embedded/integrated within a non-conductive but stretchable material. Alternatively, these types of soft strain sensors do not require specialized materials or synthesis and can be produced with conductive wire or thread. During strain or deformation of the conductive loop, the inductance of the sensor changes due to deformation in geometry of the conductive loop. Inductive strain sensors have the advantage of signal stability because they do not rely on any polymer-related properties (compared with piezoresistive and capacitive strain sensors). Since inductance is a property related to the magnetic field strength of conductive material, electromagnetic noises and disturbing interferences can affect the signal obtained. In order to achieve a sufficient signal with excellent signal stability, inductive sensors can encompass large areas, use multiple coils and change the magnetic permeability of the material [21]. Textile-based inductive sensor technology has a discounted value compared to piezoresistive and capacitive sensors and has yet to be used for multi-axis kinematic motion tracking [43], [56].

3.1.4. Existing inductive-based strain sensors

Previously, wearable inductive-based motion tracking sensors have been developed by enclosing an area with conductive thread or wire and have been used to track motion in a single axis including joints such as the elbow or knee [21], [23], body posture [57] and skin deformation [58]. The sensing mechanism of an inductive sensor relies on a change of geometry; when loops have created the change in area results in a change in inductance. Inductive sensors have the advantage of signal stability over prolonged periods since they do not rely on any specific polymer-related mechanical properties (compared with piezoresistive and capacitive sensors). To achieve a sufficient signal with high sensitivity inductive sensors can encompass a larger area, use multiple coils [21], [58] and change the magnetic permeability of material used in the sensor [21]. Textile-based inductive sensor technology seems to be under represented compared to the more popular piezoresistive and capacitive sensors and has yet to be any used for

multi-axial kinematic motion tracking [42], [43]. There has also been recent interest in utilizing analogous soft-sensors for robotic perception, an area that could also benefit from inductive sensing capabilities [59].

Inductive strain sensors have been fabricated in various ways in order to achieve a change in signal for a change in geometry. It was attempted to embed copper wire in the form of a rectangular loop into silicon rubber to obtain high stretchability (up to 120% strain) while directly being attached to the skin to monitor skin deformation [60]. Despite the approximate linear correlation achieved in this method of fabrication, this method resulted in low sensor inductance at no pre-strain (strain = 0%) with a value of no more than 300 nH. The sensor's inductance during operation can make it difficult to be used in daily life under non-controlled environments as there are various electromagnetic fields (such as the human body) as well as ferromagnetic objects such as smartphones, metallic objects, etc.

Because inductive-based sensors will respond to a change or deformation of geometry, they are not limited to strain only for operation. Inductance changes upon deforming the conductive loop without necessarily stretching, such as bending, even using non-elastic material in fabrication. An attempt was made to track the elbow angle by placing a non-stretchable inductive sensor on the deforming segment of the joint angle, such as on the median cubital vein area [22]. In this configuration, elbow joint angle and inductance signal variation were found to be correlated non-linearly.

Configuring conductive loop in a garment using standard knitting techniques could also be another option for embedding inductive-based sensors into a garment. Using a knitting machine and introducing other conductive material to increase magnetic permeability, it was possible to fabricate an arm sleeve consisting of two significant coils [21]. Although the coils consisted of a various number of loops to achieve an improved signal, the porotypes fabricated were able to track single-axial joint movement.

3.2. Basic Requirements

In addition to small-size, comfortable (i.e. non-invasive), ideal strain sensors must be durable as they undergo frequent strain cycles. Moreover, tracking specific movements such as those on the lower body requires sensors to monitor motions up to a certain speed

and frequency. For instance, sprinter's gait cycle during running can be up to 5 Hz during running [61]–[64], although the human body can move at a frequency beyond 10 Hz in certain circumstances such as seizures [65].

Tracking motions at higher frequencies can be strenuous for common piezoresistive sensors because of hysteresis and rate-dependence effect. However, inductive sensors should not be susceptible to these adverse effects and theoretically should track fast frequency movements efficiently [47], [48], [66].

Thus far, there have not been numerous studies on inductive-based strain sensors compared to resistive and capacitive ones. Among inductive-based soft strain sensors, there have been no attempts to fabricate and characterize high-inductance (a few μH) soft inductive strain sensors that require no knitting technique and/or chemical process for fabrication. These sensors may be required to occupy only up to a small area (a few centimeters in length) in order to be integrated into garments used in everyday life. Additionally, a significant portion of resistive-based soft sensors developed suffer from long-term signal stability, which might be caused by the chemical processes during fabrication.

Chapter 4.

Inductive-Based Strain Sensor's Fabrication and Characterization

4.1. Fabrication of a spring-inspired soft inductive-based strain sensor

The sensor in this study was fabricated, considering previous works available in the literature. An essential aspect of inductive-based strain sensors is their sizes, given that they can be easily integrated into everyday garments if not exceeding a specific size limit in dimensions. Also, the self-inductance of the sensors must be high enough in order to reduce magnetic disturbances from other sources, which would increase the size of the sensor. Otherwise, the sensor should be able to be fabricated, having multiple loops of conductive material. Additionally, in order to make the fabrication process at low-cost as well as reproducible, any chemical process was avoided during sensor fabrication.

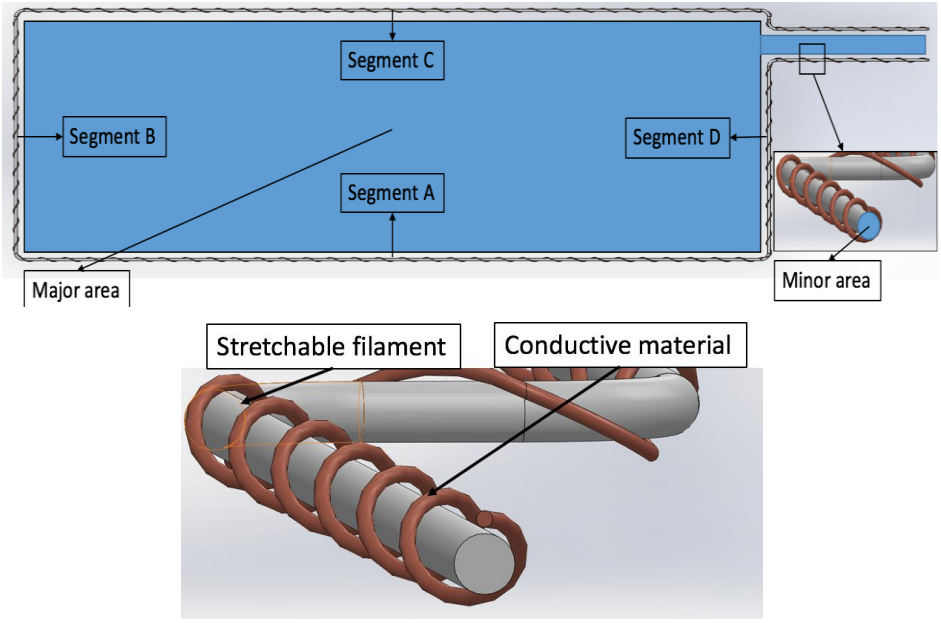

Figure 4.1 **Copper coiled elastic thread: main components and illustration of major area encircled by major loop and minor area encircled by the minor loop (solenoid) of a simple one-loop sensor where each segment is a solenoid.**

Springs—commonly used in different mechanical structures for force/shock absorption—was an inspiration in the inductive-based sensor fabrication because of their durability and flexibility. In order to have a comfortable smart garment equipped with strain sensors, the maximum force required to be applied to strain sensors to obtain sufficient signal variation should not exceed the force applied to a stretchable garment's textile during everyday use. In other words, if these sensors require a sturdier force to deform them, it would likely make them uncomfortable for the users to wear, or a sufficient signal cannot be obtained during operation. Therefore, the thinnest most conductive materials among all accessible, low-cost commercially available conductive materials—thin copper wire (72 μm in diameter)—were chosen. Because such thin copper wire thread is easily bendable (a spring of such wire would deform upon loading or unloading), a stretchable thread (850 μm in diameter) was introduced into the fabrication process as mechanical support. This made it very similar to elastic conductive wire design [67] used for data and power transmission.

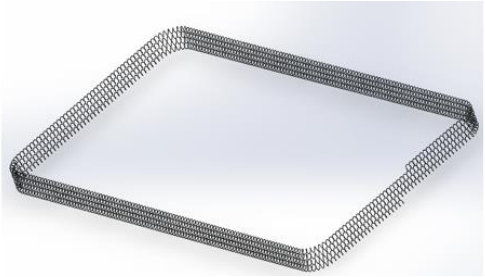

Figure 4.2 3D model of a sample sensor patch consisting of three loop.

Figure 4.3 A fabricated 3-loop sensor sample.

Having such a mechanical structure, it was possible to change the pitch value of the minor coil (spring) as well as increasing the number of loops in the major coil. To fabricate the copper coiled elastic thread (CCET) as shown in Figure 4.3, a custom-made spur machine made in MENRVA lab was used whose simplified illustration is available in Figure 4.4. The fabrication machine consisted of four rotary actuators, three pulling the

elastic thread along a guided path and another rotary actuator spurring the thin copper wire around the elastic thread, creating the CCET (spring). The CCET was used to form rectangular loops using a zigzag sewing stitch. This patch sensor (Figure 4.2 and Figure 4.3) could be constructed to have variable size and number of loops. The variable size resulted in the ability for the sensor to be used in different applications requiring different sensor dimensions.

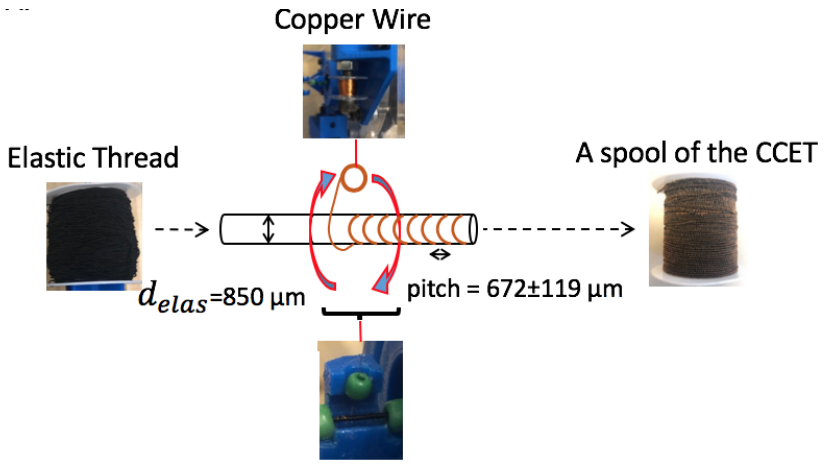

Figure 4.4 Illustration of fabrication process of copper coiled elastic thread.

4.2. Sensor's raw data acquisition

With the exception of section 4.3 (where inductance was measured directly with Keysight E4980A Precision LCR Meter), in all tests presented, an LDC1614 four-channel 28-bit Inductance to Digital Converter for Inductive Sensing by Texas Instruments was used to measure the sensor signal. The LDC1614 chip was interfaced via an I2C protocol using a STM Nucleo-F401RE, which was programmed to set proper register values (Appendix A, Table A.1) at the beginning of each trial, read the corresponding registers, and convert sensor's raw output from bits to decimal values for each sensor. According to LDC1614 datasheet, the decimal values obtained for each sensor can be used to calculate the frequency of the current generated in the LC circuit, which then can be converted to inductance. For simplicity, the decimal values of each sensor's raw signal were used throughout this investigation.

$$f_{sensor}(t) = \frac{DATAx * f_{REFx}}{2^{28}} \quad 4.1)$$

$$L(t) = \frac{1}{\left(2\pi \cdot f_{sensor}(t)\right)^2 \cdot C} \quad 4.2)$$

According to LDC1614 Datasheet, formula (4.1) shows the relationship between measured frequency of the sensor and the raw signal in bits, where $DATAx$ is the raw signals in bits measured in each sensor (x). f_{sensor} is the sensor's oscillation frequency calculated in Hz, f_{REFx} is the reference frequency (set to 40 MHz) in the chip, $L(t)$ is the inductance in Henries at time (t) and C is the sum of sensor's capacitance and parasitic capacitance. The parasitic capacitance of the coil is negligible in comparison to the selected capacitor, which was 330 pF and chosen to match the inductance [58] –in order to obtain a stable reading. In tests where a relative change of inductance value of the sensor was necessary but not the absolute values, the LDC1614's raw output in decimals were used as well as during final data collection among 12 healthy participants. A list of configurations for registers is available in Table A.1.

In section 4.3, an LCR device was used to measure inductance. The device was set at a reference frequency of 100 MHz and 5 mV, which were found to be the best fitting parameters producing stable (observing the less noise in reading) measurements after trying a few possible options. The parameters included reference frequency of 1MHz, Level (voltage) of 0.5V and auto range mode.

Except for section 4.3, in all other sections, the sensor's signal was measured using the LDC1614 chip, which measures the sensor's oscillation frequency (f_{sensor}). The value of the f_{sensor} is affected by C and L according to formula (4.2). Throughout this investigation—and similar to other works [58]—the capacitance of the sensor keeps invariant while the inductance changes as a result of a change in strain, except for section 4.6.7, which will be discussed later in this chapter.

4.3. Sensor's principle of operation

There have been various attempts to investigate the electromagnetic field and self-inductance of inductive coils as they are commonly used in various electronic circuits. In other words, it is highly beneficial to choose certain geometric parameters, such as dimensions, area and volume of a coil, given a confident expectation. Similarly, it can be very valuable to derive a mathematical formula of the strain sensor.

Opposite to piezoresistive, inductive-based strain sensors—which are usually in the form of an inductive coil—can be modelled using mathematical formulas for inductance calculation available in the literature. However, before reaching this, it is crucial to understand why inductance is expected to change upon applying strain to an inductive sensor fabricated in this work.

The sensor in **Error! Reference source not found.** can be viewed as a coil made of copper wire with a diameter of 72 μm forming at least one rectangular loop (major loop). Each segment of the rectangular loop is made of solenoid (minor loop) in order to allow the sensor to be loaded (stretching the sensor) and unloaded (the sensor shrinks back to its original state) in different directions without a breakage since the copper wire is not elastic. Each solenoid (minor loop) is parametrized by pitch value, length, inner area (minor area) and the number of loops.

Since the sensor was fabricated with the aim of finally being used in a hip joint monitoring prototype, the parameters of the sensor such as width, length, i.e. were chosen, considering requirements observed in the final prototype. Determining other parameters related to sensors, such as pitch value, minor area (the area bounded by solenoid's loops, i.e.) was limited by the available materials and methods of production. Due to an optimal number of sensors required to be on the prototype device, which will be discussed in section 4.4, the size of the sensors could not exceed more than 10 cm in length and up to 4 cm in width. Additionally, the pitch value was limited by the custom-made spur machine available in MENRVA lab. Finally, the number of major loops that were empirically found to produce sufficient inductance in the non-loaded state of the sensor was three (3), which will be discussed later in this chapter. Throughout the tests conducted in this chapter, sensors in two different sizes were used to provide an insight of behavioural differences that might be resulted due to changing the size of the sensor, if any. Later in the chapter, it is concluded that the sensor's primary behaviour (inductance-strain) is similar in both sizes.

- pitch value: 672 ± 119μm
- spandex diameter: 850 μm
- number of major loops: 3

- diameter of copper wire: 72μm
- Sensor A: 40.7mm X 20.0mm with no base fabric
- Sensor B: 106.1mm X 40.0mm with base fabric (similar to smart shorts prototype explained in Chapter 5)

4.3.1. Inductance of a small-sized solenoid

To begin with, assuming that strain is applied along the direction of the rectangle's length, the pair of rectangle's solenoids loads which causes the pitch value to increase, the minor area to decrease and the length of the segments (solenoids) to increase. To calculate inductance of conventional solenoids, its geometric parameters as well as the near space permeability can be used [68]. However, when inner-turn spacing of the solenoid is not negligible, a correction factor *K* needs to be used [69]. From self-inductance of solenoids we have:

$$L_{solenoid} = \mathrm{K}\frac{\mu_0 N_{solenoid}^2 A_{minorArea}}{d}[69] \quad 4.3)$$

Where, $L_{solenoid}$ is the self-inductance of a solenoid in Henries, μ_r is relative magnetic permeability constant ($4 \cdot \pi \cdot 10^{-7}$H/m), $N_{solenoid}$ is the number of turns in a solenoid, $A_{minorArea}$ is the area of the minor loop's cross-section, and d the solenoid's length. After applying *K*, the inductance-area and inductance-length relationships will remain unchanged.

It is possible to show that the sensor's change of inductance is majorly caused by the increase of major area (**Error! Reference source not found.**) encircled by the loop while the inductance of its helical segments (solenoids) decreases only slightly compared to the increase caused by the changing major area.

A study which aimed to propose a novel design for an LC strain sensor for sensitivity enhancement, have illustrated how inductance of a solenoid is decreased upon applying strain [69]. Later, they suggest a novel design which aims to improve the sensitivity. In this study, the measured equivalent inductance of a solenoid with similar pitch/coil_diameter ratio (0.22) compared to that of our sensor (0.79), was decreased by 0.129 μH (obtained from their LC parameters and formula 4.1) upon applying 7% strain

(1.84 μH for 100% strain). This shows that inductance of a small-sized solenoid is decreased upon applying strain (increasing the coil's length). However, this inductance variation can be different for a coil with different length, diameter and conductive wire's thickness, given a similar pitch/coil_diameter.

To calculate the inductance variation of a solenoid, Lorenz solenoid current sheet formula was used and initially validated using the previous study's recorded measurements [69]. Using this formula and dimensions of the sensor available in [69], for 7% strain, 0.095 μH inductance variation is obtained, which still shows an underestimation of inductance variation compared to the results recorded in the measurement (0.129 μH). Using our sensor's dimensions, the calculation leads to a change of 0.010 μH for 100% strain. Later in section 4.3.2 and 4.3.3, it is shown that the inductance variation as a result of change in the major area is much larger than that of caused by each solenoid's change in length.

Assuming the 'almost' rectangular loop (neglecting fillets at the corners) to be an ideal rectangle, similar to the approach used in numerical inductance calculation for a rectangular loop based on first principle [70] as well as calculation of self-inductance of a strain sensor [60], the total self-inductance of a single-loop sensor (one rectangular loop made of solenoid segments) is:

$$L_{sensor} = 2(L_{length} + L_{width}) - M_{oppositeSides} \tag{4.4}$$

$$L_{sensor} = 2\big(L_{length} + L_{width}\big) - (M_{A,C} + M_{B,D}) \tag{4.5}$$

Where L_{sensor} is sensor's total self-inductance, L_{length} is the self-inductance of length segment (i.e. segment A), L_{width} is the self-inductance of width segment (i.e. segment B) and $M_{oppositeSides}$ is the mutual-inductance of every two parallel but opposite (the reason for negative sign) segments of the loop (i.e. sum of mutual-inductances between segment A and segment C and that of B and D $(M_{A,C} + M_{B,D})$). Also, since segments A,B and C,D are located perpendicular with respect to each other, their mutual-inductance is considered zero [60].

When the sensor is loaded in direction of sensor's length (during positive strain), L_{width} and $M_{B,D}$ stay constant, L_{length} decreases and although $M_{A,C}$ decreases, but because

of the negative sign (opposite current running in two segments), the term $-M_{A,C}$ increases. Therefore, the relationship between strain and inductance in this configuration is dependent on the rate of change of the named two terms, $-M_{A,C}$ and L_{length}(i.e. if the increase of inductance due to $-M_{A,C}$ overcomes the decrease of inductance caused by L_{length} or vice versa). In case of a multi-loop circle, the effect of $-M_{A,C}$ is amplified (due to having multiple parallel segments with current running in opposite direction) as well as introducing positive mutual inductance ($+M_{A,A'}$) as a result of having multiple parallel segments with current running in the same direction.

4.3.2. Inductance as a function of the loop's dimensions

For simplification, each solenoid constructing each segment of the loop was approximated to a straight line resulting in a loop of rectangular shape made of round wire. Using formula (4.6) available in literature [71], it is possible to calculate self-inductance of multi-loop rectangular loop:

$$L = \frac{\mathrm{N}^2\mu_0}{\pi}\left[x\ln\left(\frac{2x}{r}\right) + y\ln\left(\frac{2y}{r}\right) + 2\sqrt{x^2+y^2} - x\sinh^{-1}\left(\frac{x}{y}\right) - y\sinh^{-1}\left(\frac{y}{x}\right) - 1.75(x+y)\right] \quad (4.6)$$

Where x and y are width, length of the rectangle and r is the radius of the wire's cross-section and N is the number of loop (turns) in the rectangle.

In a test using a stress-strain device Instron E10,000 (Norwood, MA, USA), an LCR Meter (Keysight E4980A Precision LCR Meter, connected to a running MATLAB) for measuring Inductance of the sensor during the test, the sensor was loaded and then unloaded up to 100% strain. The sensor's inductance was measured and compared with the results obtained from formula (4.6), which is shown is Figure 4.5/B. To compare the signals in a relative manner, the signals were normalized (Figure 4.5/C) using formula (4.15) and (4.16). As sensor A was used in section 4.3.2 and 4.3.3 and there was no base fabrics involved, the fabrics Poisson's ratio was considered zero.

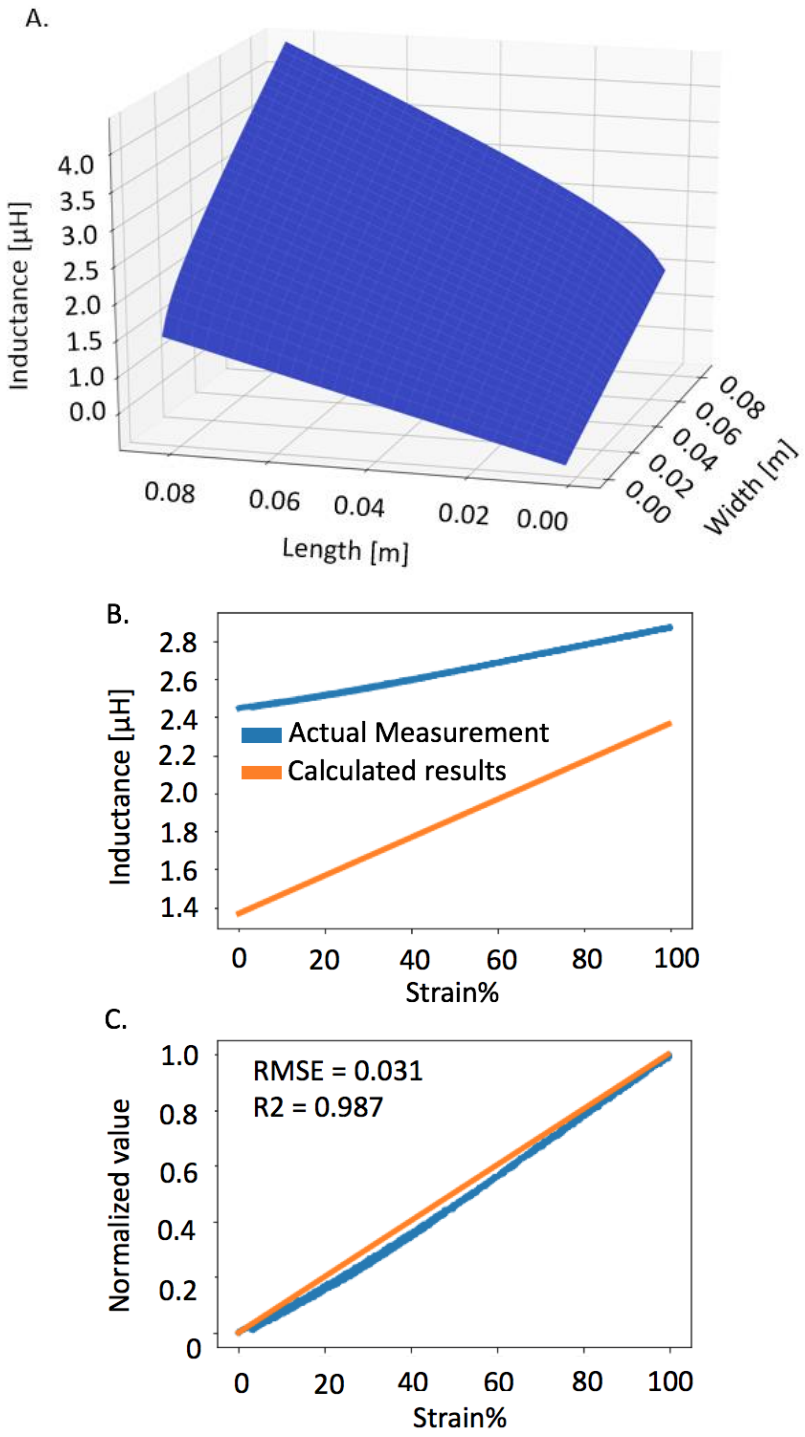

Figure 4.5. **A) Inductance as a function of length and width of a rectangular loop in the rectangle-based loop. B) Actual measurements obtained from LCR during 0%-100%-0% strain cycle versus calculated results. C) Normalized data presented in B) which shows NRMSE and R^2 between actual and calculated results.**

4.3.3. Inductance as a function of loop's area and perimeter

As an alternative approach, the sensor can be viewed as a polygon made of conductive material (copper) with circular cross-section, if segments consisting of solenoids are treated as straight lines. The self-inductance of polygon is calculated using the formula below [21],[22]:

$$L_{polygon} \approx \frac{\mu_0 P}{2\pi}\left[\ln\left(\frac{2P}{r}\right) + 0.25 - \ln\left(\frac{P^2}{A_{majorArea}}\right)\right] \quad (4.7)$$

Where $L_{polygon}$ is inductance (H), P is perimeter (m) of the loop, $A_{majorArea}$ is the area (m^2) encircled by the loop, and μ_0 is relative magnetic permeability ($4 \cdot \pi \cdot 10^{-7}$H/m).

The area can be approximated by a rectangle with length *l* and width *w* ($A_{majorArea} = l \cdot w$). Considering the spring as a constructing element of the rectangle as shown in **Error! Reference source not found.** the perimeter of the sensor's loop (P_{spring}) can be approximated by:

$$Number\ of\ turns\ in\ the\ spring = \frac{l}{pitch} \quad (4.8)$$

$$Perimeter\ of\ the\ spring\ with\ 1\ turn = \pi \cdot d_{span} \quad (4.9)$$

$$P_{spring} = \frac{l}{pitch}(\pi \cdot d_{span}) \quad (4.10)$$

Where d_{span} is diameter of spandex (the elastic thread) and, and *pitch* is the distance between each coil (within each segment of each loop, **Error! Reference source not found.**). Therefore, the perimeter of the sensor or length of copper wire present, would be:

$$P_{sensor} = 2 \cdot \left(\frac{l}{pitch} \cdot \pi \cdot d_{span} + \frac{w}{pitch} \cdot \pi \cdot d_{span}\right) = \frac{2 \cdot \pi \cdot d_{span}}{pitch} \cdot (l + w) \quad (4.11)$$

This formula (4.11) was used for approximating the inductance of the sensor based on its geometric parameters. Finally, the formula for calculating inductance as a function of its length can be derived as follows, assuming that the strain was applied in direction of the length of the sensor according to [71]:

$$L \approx \frac{\mu_0 P_{sensor}}{2\pi}\left(\ln\left(\frac{2P_{sensor}}{r}\right) + 0.25 - \ln\left(\frac{P_{sensor}^2}{w}\right)\right) + \frac{\mu_0 P_{sensor}}{2\pi}(\ln(l)) \quad (4.12)$$

Given that all parameters are constant except *l* in formula (4.12), the sensor's inductance correlation is non-linear with a changing length of the sensor defined by the natural logarithm function.

Similarly, when having a multi-loop sensor with *N* as number of loops, the perimeter of the sensor or the amount of copper wire present in the loop is multiplied by *N.* Finally, the area bounded by the loop is multiplied by the number of loops as well which results in following (depicted visually by Figure 4.6/A):

$$L_{multi\ loop} \approx \frac{N\mu_0 P_{sensor}}{2\pi}\left(ln\left(\frac{2NP_{sensor}}{r}\right) + 0.25 - ln\left(\frac{(NP_{sensor})^2}{Nw}\right)\right) + \frac{N\mu_0 P_{sensor}}{2\pi}(ln(l)) \quad (4.13)$$

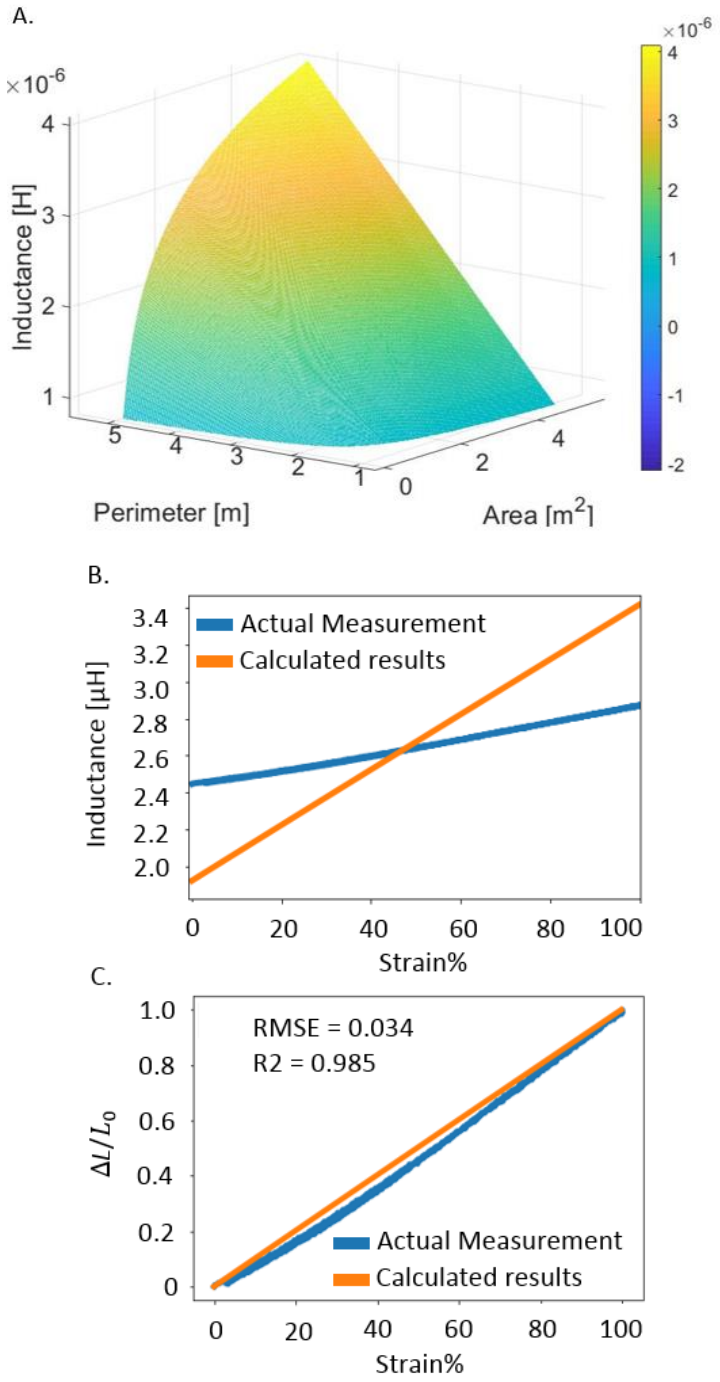

Figure 4.6. A) Inductance as a function of area and perimeter in the polygon-based loop. Graph B) Actual measurements obtained from LCR during 0%-100%-0% strain cycle versus calculated results. C) Normalized data presented in B) which shows NRMSE and R^2 between actual and calculated results.

As demonstrated in Figure 4.5/B and Figure 4.6/B, using either formula (4.6) or (4.13) resulted in an underestimation of the base inductance value but overestimation of

the gauge factor (change in inductance versus change in strain). The underestimation might be originated by using the two approximating formulae for inductance calculation which were developed for polygon-shaped loops. The overestimation of gauge factor can be a result of not considering the inductance change of solenoidal segments (A,B,C and D) and mutual-inductance of each pair of segments (A and C) which can change at a different rate with respect to length. In both models, the sensors solenoidal segments were approximated by a line which could be the main reason for the discrepancies in absolute values measured by the LRC Meter and formula (4.6) and (4.13). Despite this disagreement, the relationship between strain and inductance is shown to be pseudo-linear (Pearson ratio: 0.99) and is in fact in agreement with the data obtained from the 0-100% strain test.

4.4. Method for Real Application Strain Range Calculation

Since the sensors were eventually meant to be used in a wearable garment to monitor the hip joint angle in three dimensions, it was important to determine the range of strain and strain rates, the sensors will be operating at, before conducting sensor tests. This requires first to determine and choose the locations where the sensors are to be installed, as the location of the strain sensors on a stretchable garment can affect the performance of the system [44], [45]. The exact locations for an ideal strain sensors—where strain data obtained from optical motion capture system were used as candidate strain—were found for tracking hip joint angle during running [46]. The OMC could output the absolute position of the markers, which can be converted to strain over a certain area. These were the locations where strain patterns and range were found to be the most valuable sources of information for a machine learning model for various sensors. In this study [46], it was found that using more than four sensors did not result in significant improvements in accuracy. Also, the LDC1614 chip used for the data collection on a population of 12 participants, was capable of reading a maximum of 4 sensors which—for simplicity of the prototype—determined the number of sensors to be used on the final prototype.

The location and orientation of the sensors in the final prototype followed the suggested locations, as found by M. Gholami et al. [46]. However, the size of the sensors used in this garment was approximately 9 cm in length and 3 cm in width. This dimension was empirically found to be more informative to the machine learning model used for

mapping the sensors data into the hip joint angle and resulted in relatively higher accuracy in measuring hip joint angle in the transverse plane. The final placements of the sensors are shown in Figure 4.7/B/C.

Two optical markers were attached using fabric fusion tape at each end of each sensor to measure the strain applied to each sensor during two minutes of a participant's running at a speed of 2.0 m/s (same protocol as in main data collection), presenting an insight into what the range of strain was applied to each sensor during running. The configuration of the motion tracking markers is shown in Figure 4.7/A. The maximum strain applied to any sensor did not exceed 28%, including the pre-strain (10%) applied to the sensors when the garment was worn compared with its unworn state. Therefore, the maximum working range for the sensors tested was considered 30%. This test was intended only to determine the sensing range of the strain sensors and give an insight into the strain rates applied to each sensor during running. This test protocol indeed independent from the test protocol used during cohort testing (Chapter 5).

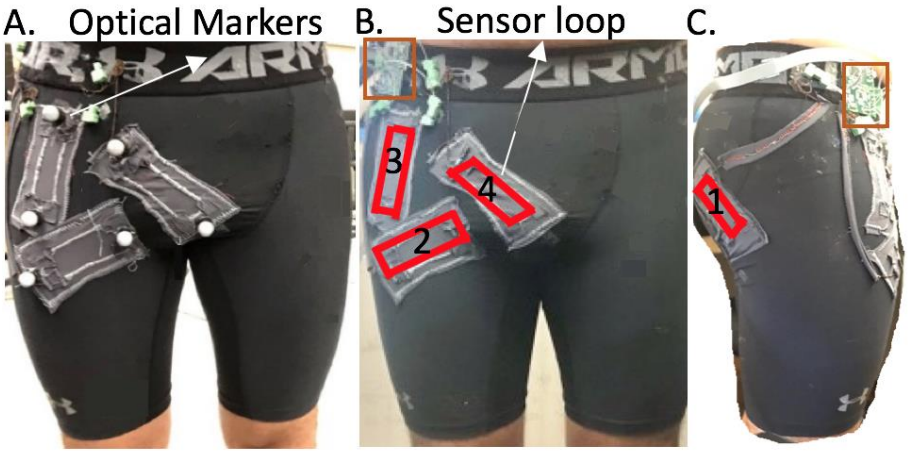

Figure 4.7. A) Optical marker placement for strain range determination. B) red boxes represent the position of the sensors C) orange box represents the placement of the LDC1614 board.

After determining the tensile test working range of the strain sensors incorporated into the garment, the strain rates experienced by each sensor was studied during the two-min running test. As the histogram in Figure 4.8 shows, some sensors experienced a strain rate of up to 150%.s^{-1}, but the majority were among 50%.s^{-1}. Thus, it is important for the strain sensor to be able to track high speed strain changes during activities. A separate section for frequency and strain rate tests was allocated to study this ability which will be discussed later in this chapter.

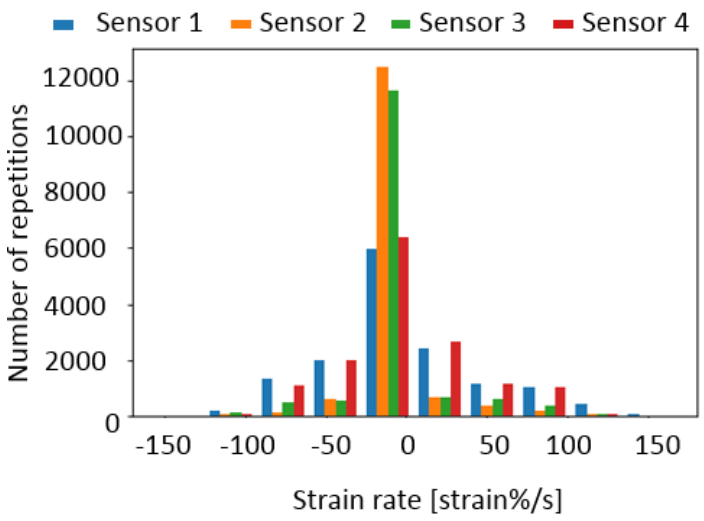

Figure 4.8. Strain rate histogram of each sensor used in smart shorts during 2-min running.

4.5. Normalization and evaluation metrics definition

The data acquisition system for the linear stage testing recorded displacement of the actuator with respect to its original position in one axis. Displacement was converted to strain at each moment in time using formula (4.14). Python 3.6 and the formula below were used to normalize strain and the sensor's raw signals.

$$S(t) = \frac{displacement(t)}{l} \tag{4.14}$$

$$S(t)_{normalized} = \frac{(S(t) - S_{\min})}{S_{max} - S_{\min}} \tag{4.15}$$

$$f_{bits}(t)_{normalized} = \frac{(f_{bits}(t) - f_{bits_{\max}})}{f_{bits_{min}} - f_{bits_{\max}}} \tag{4.16}$$

Where $f_{bits}(t)$ is the signal value at time t; f_{min}, S_{min} are the minimum value of that raw signal and strain in each trial, respectively; f_{max}, S_{max} are the maximum value of the raw signal and strain, respectively; $f(t)_{normalized}, f_{bits}(t)_{normalized}$ are the normalized value of the raw signal and strain in time t, respectively. The statistical analysis was completed to determine the RMSE between the strain signal and resulting inductance signal. The result was multiplied by 100 to give a percent to two decimal places.

4.6. Tensile Tests

4.6.1. Sensor testing: Step test

In order to achieve a better understanding of the sensor's performance, the electro-mechanical properties of the sensor were investigated with respect to different strain profiles. The sensor was initially analyzed by completing strain-inductance measurements to determine the signal quality and accuracy within our desired working range (<30% strain, discussed in section 4.4). The sensor was able to track steps in 5% increments from 5-10-15-20-25-30-25-20-15-10-5% strain at 1%/s with 10 second holds at each step and resulted in an NRMSE = 2.83% (Figure 4.9). The step holds did not show any signal drift/relaxation.

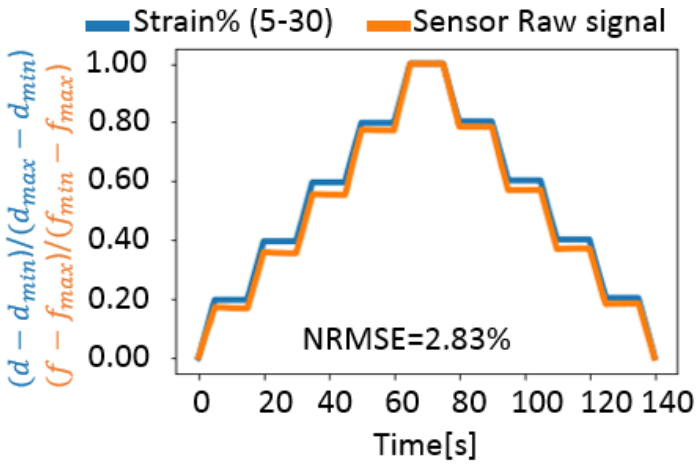

Figure 4.9. Normalized step test result using sensor B from 5% to 30%.

4.6.2. Sensor testing: hysteresis and gauge factor

To check the hysteresis and any time-dependent effects a triangular wave pattern with increasing strain (0-1-0-2-0-3-0…30-0% strain at 5 mm/s) was completed. The sensor was able to track with an NRMSE = 1.43% (Figure 4.10/A). There was no change/drift in the baseline and/or peak values and the sensor displayed no hysteresis (Figure 4.10/C), represented as an inductance vs. strain plot in Figure 4.10/A. The sensor displayed a consistent gauge factor (GF) of -0.055±0.002 from 0-30% strain (Figure 4.10/B). GF was defined as:

$$GF = \frac{\Delta f / f_o}{\Delta l / l_0} \tag{4.17}$$

Where Δf the change in frequency of the current was generated in the LC circuit, f_o was the initial frequency of the current in the LC circuit at 0% strain, Δl was the change in length, and l_0 was the initial length of the sensor.

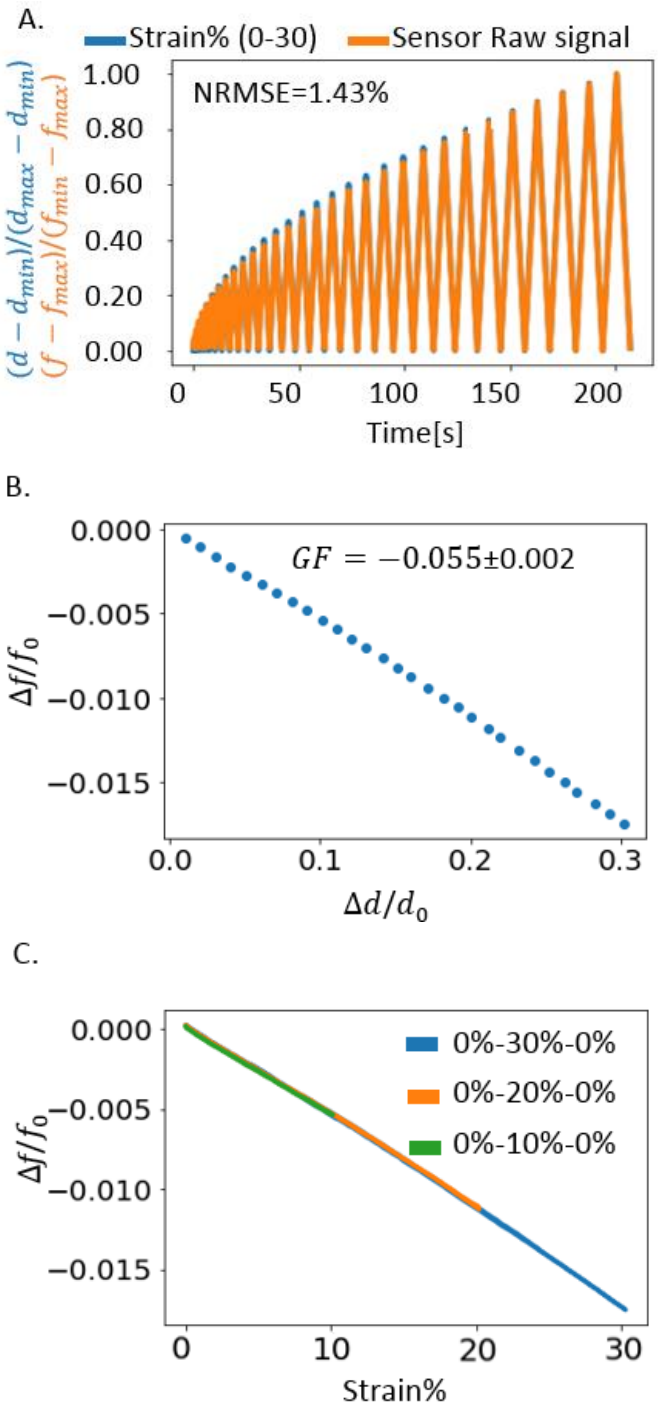

Figure 4.10. **A) Triangular wave pattern from 0-30% strain in 1% increments. B) The linear relation of $\Delta f/f_0$ and $\Delta l/l_0$ and the gauge factor (GF) up to 30% strain. C) Hysteresis plot from 0-10-0%, 0-20-0%, and 0-30-0% strain.**

4.6.3. Sensor testing: signal drift and noise

The sensor stability was analyzed over a period of 10,000 seconds (2.7 hours) with a minimal constant strain (0.1%). The sensors signal had a maximum signal drift of 0.48% (0.00077 MHz, Figure 4.11, largest signal deviation) and a signal noise calculated at three separate 1-minute intervals of 0.05% (0.00016 ±0 0.0001 MHz, Figure 4.11, green boxes left to right). A noteworthy difference between the drift of this inductive sensor versus a capacitive and piezoresistive sensor was that the drift was very minimal (equivalent to 0.48% strain) and did not follow a specific pattern such as constant increase or decrease. Typically, for piezoresistive and capacitive sensors, the drift is permanent and follows a specific pattern.

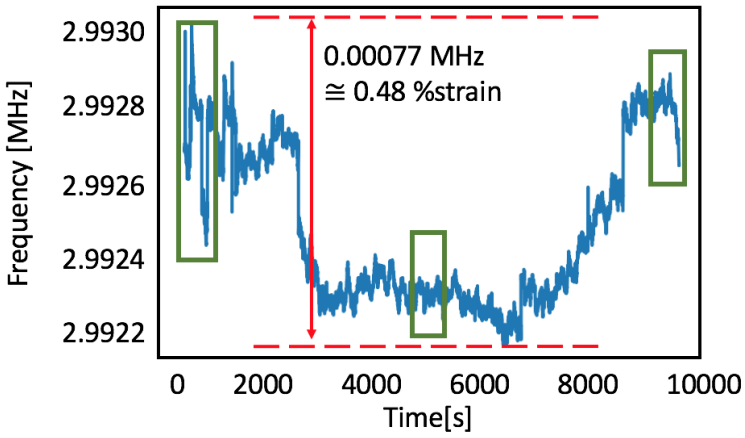

Figure 4.11. Signal variation over 2.7 hours. Green boxes represent instantaneous noise averaged on a 1-min window.

4.6.4. Sensor testing: random wave pattern tracking

The random wave test was completed by creating a random series of waypoints, with a set of boundaries from 0-6% strain and maximum strain rate of 5 mms^{-1} for one minute, with a starting load of 1.42 N. During the test, the inductive sensor was able to track with an NRMSE = 2.43% (Figure 4.12). This intended to mimic what could be observed during a prototype testing and agreed with our previous results with no under— nor over–shoot during tracking typically caused by hysteresis. The range and rate were chosen because of the limit of our custom linear stage.

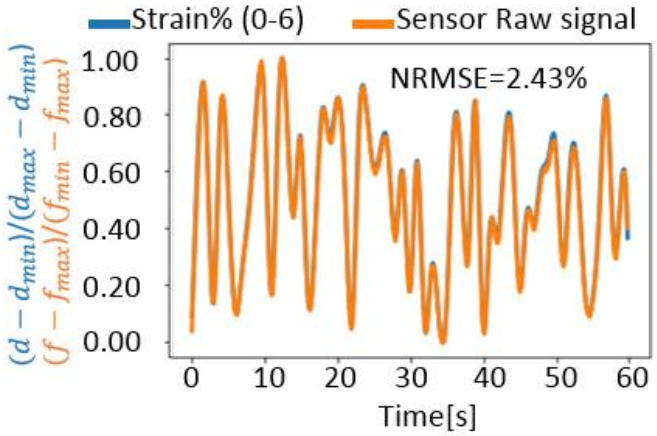

Figure 4.12. Normalized 60 second random wave pattern test.

4.6.5. Sensor testing: accurate tracking of high frequency strain

Since the speed of the Tensile device (Instron E10000 was limited to speed range), sensor A (which was smaller in length and width) was strained from 15% to 30%, over a set of 7 frequencies (0.1 Hz, 0.5 Hz, 1 Hz, 2 Hz, 4 Hz, 8 Hz, 10 Hz) each ten times with 270° phase sine waves (positive strain only). An analogous test was also completed at the limit of our instrument's capabilities with frequencies of (0.1 Hz, 1 Hz, 10 Hz, 15 Hz, 20 Hz) from 15% to 22% strain, where 10 Hz equates to 450 strain%/s, Figure 4.14/B.

Strain and the sensor's raw signal were normalized using formula (4.15) and (4.16) for comparison. The subsequent test was completed from 15-22% strain to increase the range of frequencies (Instron strain speed limitation) up to 20 Hz (Figure 4.14/A). The sensor accurately tracked the strain to 20 Hz, and only started to show a small inability for consistent peak/valley—maximum/minimums at 20 Hz. Comparing this to data obtained by optical motion tracking (Figure 4.8) the majority of motion is expected to be below 100 %/s (2 Hz in the previous test equates to a maximum of 95 %/s strain rate,), with a maximum of 150%/s—well within the ability of the inductive sensors capabilities.

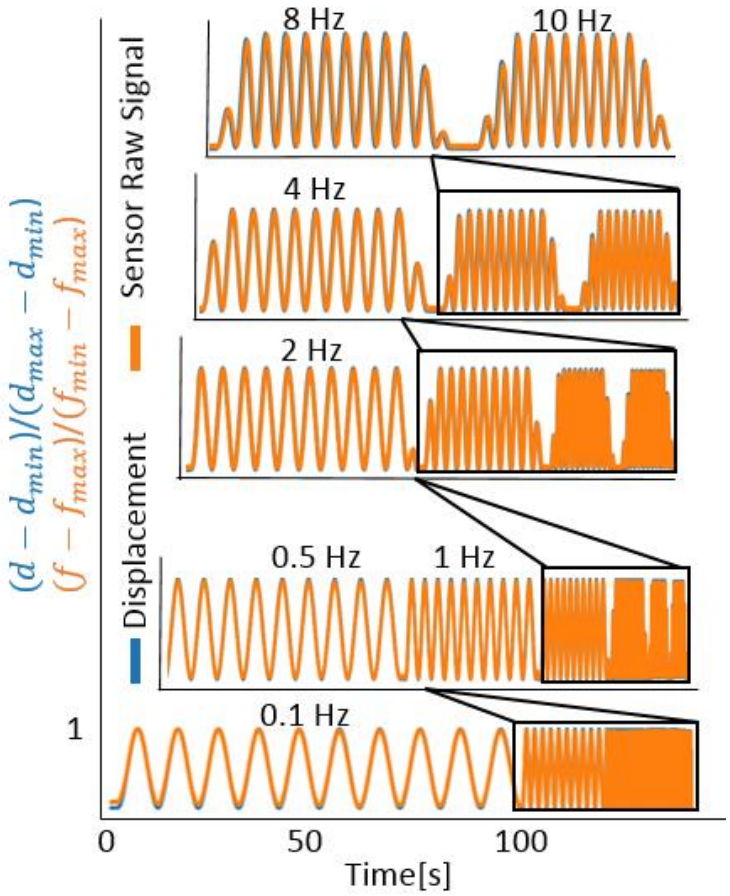

Figure 4.13. Frequency sweep up with a sine wave to 10 Hz. Displacement and sensor raw signal were normalized for comparison.

A.

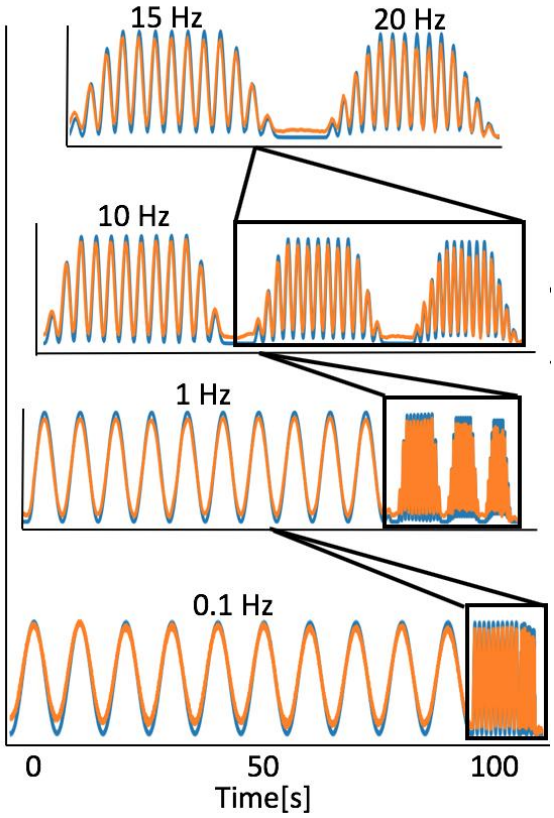

B.

Frequency [Hz]	0.1	1.0	2.0	4.0	10	20
Max Strain rate [%.s^{-1}]	4.7	47.7	95.2	186.1	452.7	403.7

Figure 4.14. A) Frequency sweep with a sine wave up to 20 Hz (404 %/s). B) Maximum (Max) strain rate [%.s^{-1}] of each frequency test.

In order to understand the effect of strain rate on hysteresis, strain was plotted against sensor signal at each frequency resulting in Figure 4.15. As Figure 4.15/A and Figure 4.15/C show, at frequencies faster than 4 Hz (186%/s strain rate), signal hysteresis was observed as a result of the mechanical lag of the CCET sensor components—likely caused by an increase in the viscous dissipation (dissipation of energy) of the elastic thread [73].

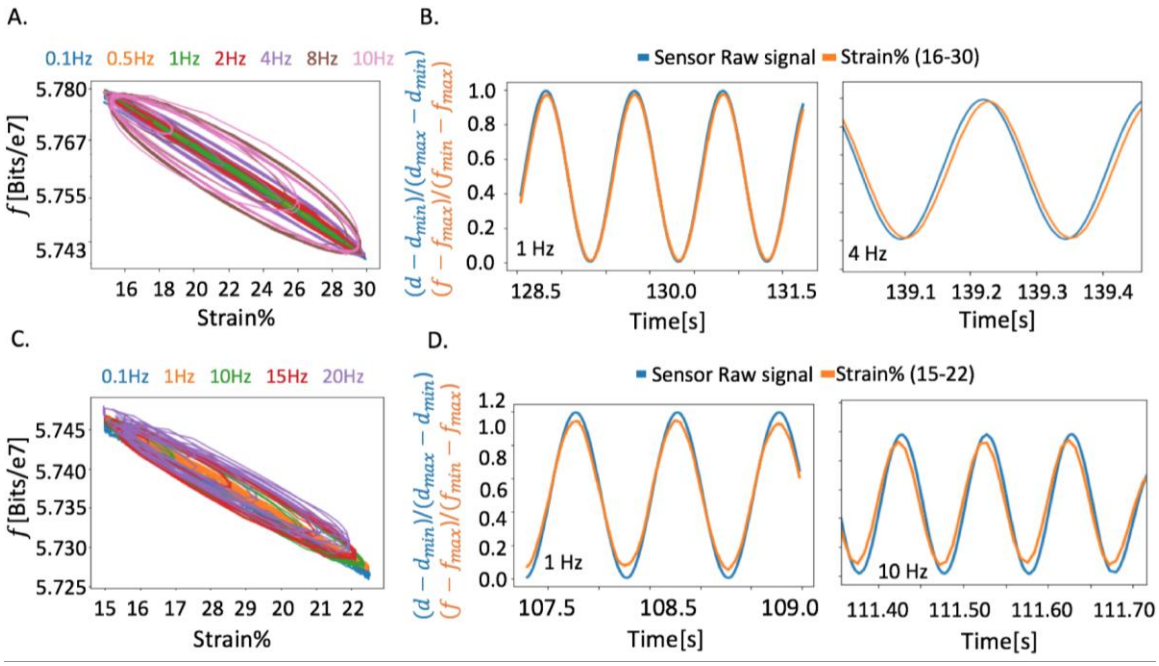

Figure 4.15. A) strain-inductance (raw signal in bits) at different frequency in frequency test 1 B) comparison between normlalized signals at two different frequencies. C) strain-inductance (raw signal in bits) at different frequency in frequency test 2 D) comparison between normlalized signals at two different frequencies.

4.6.6. Sensor testing: dynamic cyclic test

In order to investigate the performance of the sensor in a dynamic scenario, a dynamic cyclic test was conducted. In this test, sensor A experienced 300 cycles of sinusoidal strain pattern from 5%-25% (amplitude of 20% strain) at a rate of 10%.s^{-1}. Strain, stress and sensor's signal was recorded during the test and the normalized results are present in Figure 4.16/A.

The stress and sensor signal both shifted to lower values, indicating some mechanical relaxation within the sensor. The signal frequency shifted to lower values, with a consistent gauge factor. The gauge factor of the sensor during each cycle was calculated using formula (4.17). As shown in Figure 4.16/B, the gauge factor of each cycle during the test did not undergo a significant variation as a result of repetitive and consecutive test. This is a known phenomenon among some of the piezoresistive sensors [14] which can be a limiting factor towards using strain sensors in applications where repetitive movements are to be monitored.

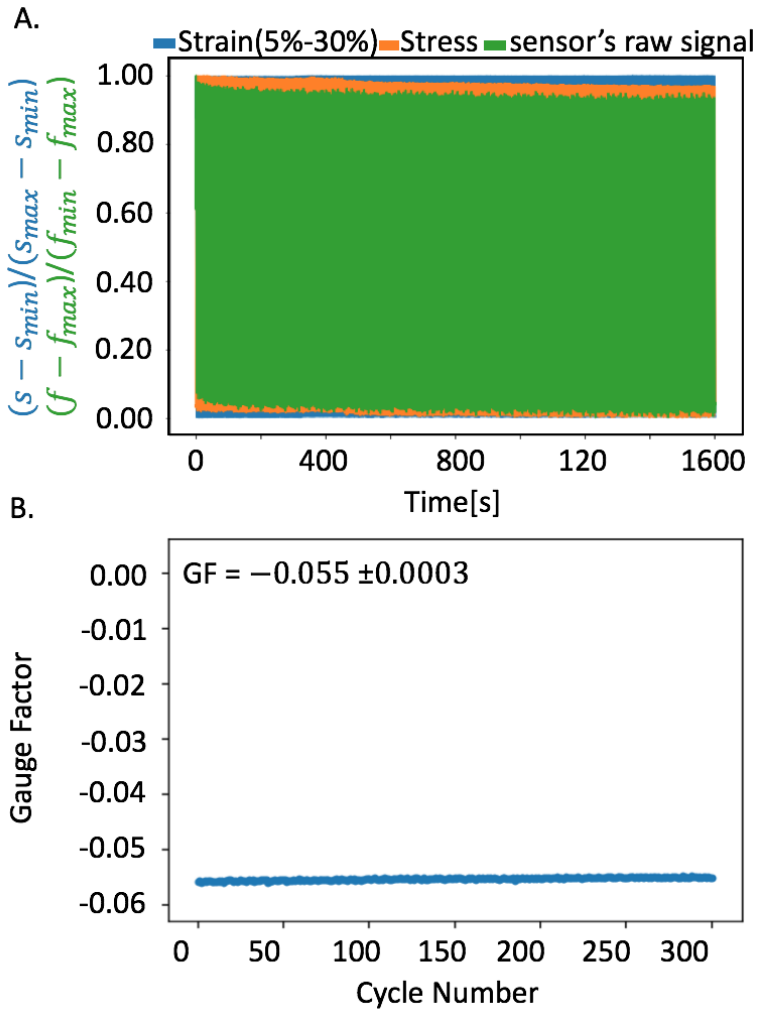

Figure 4.16. A) strain, stress and inductance result for 300 cycles at 0.1Hz. B) Variation of Gauge Factor throughout the cyclic test.

4.6.7. Sensor testing: electromagnetic sensitivity

In this test, while sensor B was kept stationary on non-metallic desk, five different items were brought to its 2 cm vicinity and away. This was repeated 5 times for each item and the sensor's signal was recorded. As Figure 4.17/A illustrates, a coin-sized magnet seemed to have the least signal interference on the sensor, only causing the sensor's oscillation frequency to change 0.002 MHz (equivalent to 0.98% strain) while the most effective interference was from an active electronic board with 0.017 MHz (10.9% strain).

In another test, in order to understand how the proximity of the two most effective object would affect the sensor's oscillation frequency, a smart phone and an active electronic board was brought to a vicinity of 0.2 cm. As shown in Figure 4.17/B, a

smartphone can change the sensor’s oscillation frequency reading, up to 0.038 MHz which is equivalent to 24.2% strain.

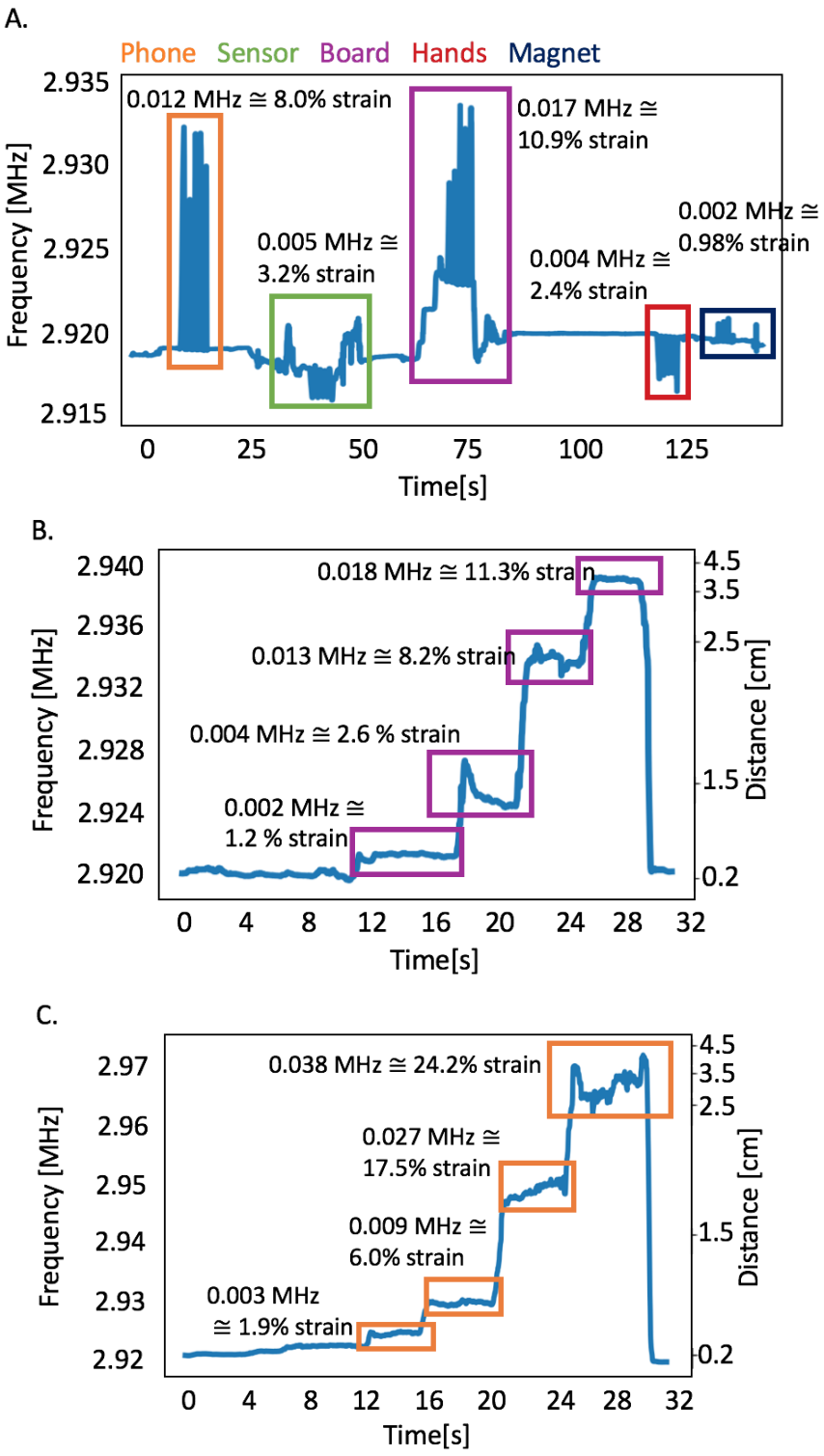

Figure 4.17. **A) Signal interference results from five objects. B) shows the effect of distance between sensor and smart phone on measured resonant frequency under 0% strain. C) shows the effect of distance between sensor and an active electronic board on measured resonant frequency under 0% strain.**

4.7. Discussion and Conclusions

There have been two approaches for causing an inductive change during strain: bending the inductive loop, without necessarily a change in area encircled by the loop and a quantitative change of area enclosed by the inductive loop [21]–[23].In these examples, material synthesis and knitting machines were required for sensor fabrications [21], [22], [60]. The fabrication method that was employed for our sensors required no material synthesis and included methods that are currently employed industrially (i.e. spur machines) and could be easily implemented to create kinematic tracking garments [69].

The sensors used in all of the sensor characterization tests as well as those fabricated for the smart compression shorts consisted of three loops around the perimeter of the enclosed area which was considerably lower than other examples that have required from 20 to 65 loops [21]. The type of conductive material and the magnetic field of the core could have an effect on the resulting performance of the sensor, although we did not explore beyond using copper wire in this work [21].

It was possible to calculate the inductance of a non-stretched sensor before choosing the geometric parameters such as width, length, and number of perimeter loops using the formulae (4.6 and 4.13) derived in previous section. The geometric parameters of the sensors were chosen such that the inductance of the sensor in non-stretched state was a minimum of 2 µH. Three enclosed loops were minimum number of loops empirically found to be insensitive to most of the electromagnetic field (EMF) disturbances of the surrounding environment—including our own bodies [74]. Choosing a smaller number of loops (e.g. 1 or 2) resulted in insufficient signal variation as well as emitting high sensitivity towards other EMFs in surrounding environment. Others have used lower base inductance values starting from a few hundreds of nH [60] to 1-3 µH [57]. As demonstrated in Figure 4.5 and Figure 4.6, using formulae (4.6) and (4.13) resulted in an underestimation of the base inductance value but overestimation of the gauge factor (change in inductance versus change in strain). The relationship to what affects the inductance base value and change will be discussed below.

The relationship of inductance to area is not formally linear (see formula (4.5) and (4.16)) and the small changes in area of the sensor result in a pseudo-linear relationship

(due to natural logarithm) within the expected working range <30% strain (Figure 4.10/C). The inductance of the sensor is a combination of:

- Self-inductance of each consisting segments. i.e. each solenoid-side of the rectangular loop
- Mutual-inductance of neighboring segments. i.e. a pair of parallel/adjacent solenoid-like sides of rectangular loop.
- Mutual-inductance of neighboring rectangular loop if more than one.

It was shown that the total self-inductance of the loop is expected to be affected by change of area of the major loop more than that of self-inductance of solenoidal segments (minor loops). Formulae 4.6 and 4.15 show that, for 0%-100% strain, an inductance variation of 1.0 and 1.4 μH due to change of major area is expected. This variation is 100-140 times more than the inductance variation due to change in length of solenoidal segments (0.01 μH, minor loop) and 40 times larger than the inductance variation measured in a 0%-100% strain test (Figure 4.5).

The sensitivity of the sensors (i.e. signal variation per 1% strain) could be improved by optimizing the dimensions and geometric parameter of the sensor—such as area, pitch value, width and number of loops—while aiming for maximizing the gauge factor. Formulae (4.6) and (4.15) can be rewritten in terms of the sensor's gauge factor and necessary variables such as those mentioned earlier can be changed in order to maximize the sensor's gauge factor. The accuracy obtained by our system is comparable with existing systems [43], [46] in terms of RMSE and NRMSE and could be clinically informative and valuable. However, for other applications or further accuracy, geometric variables can be used to enhance the gauge factor of a sensor before production.

To initially understand the effect of strain on inductance (or indirectly using frequency), tests were performed on a displacement controlled linear stage. A step test was completed from 5-10-15-20-25-30-25-20-15-10-5% strain with 10 second holds at each step (Figure 4.9). The values were consistent on the increasing and decreasing steps and did not show and signal drift/relaxation typical of piezoresistive sensors [48]. Inductive sensors and capacitive sensors are both advantageous over piezoresistive sensors in this effect, since they rely on geometric changes, not a connection-disconnection mechanism typical of piezoresistive sensors [75].

Comparing the calculated and experimental inductive signals for up to 100% strain—excluding the gauge factor by normalization—resulted in an R^2=0.985. Although the predicted gauge factor did not agree with the experimental data (Figure 4.5 and Figure 4.6), the inductance–strain relationship was in agreement. Drift of a sensors baseline signal over a period of time can be detrimental when attempting to accurately track kinematic movement over longer periods of time. The CCET inductive sensor was stable over a period of 2.7 hours to within 0.48% with minimal noise equal to approximately 0.05% change (Figure 4.11). The 0.48% change was likely from external constant and varying electromagnetic fields, such as computers, antennas and other ferromagnetic objects in the surrounding. The signal drift over time which is common among most of piezoresistive sensors, is often because of sensor's on-going interactions at molecular level, even though the sensor is at a relaxation state. Since the inductive sensor do not go through any chemical process during production, such as coating, layer depositions etc. the materials are passive chemically. Only, the geometry of the sensors as well as other significant electromagnetic fields can influence the sensor's readings. The small gauge factor of the sensor is offset by stable reproducible signal with low noise. The sensors basic characterization results were promising prior to device (smart sport shorts) production displaying accurate and reproducible tracking that is required for motion tracking.

Another characteristic that affects piezoresistive—and to a lesser degree capacitive—sensors is hysteresis [75]. Since our inductive sensor relies on the area enclosed by the coiled loops, and was created with an elastic core, there was no hysteresis within our working range < 30% strain (Figure 4.10/C).

The sensor's signal is measured by measuring its oscillation frequency which can be affected by both capacitance and inductance of the sensor (formula 4.2). In a test where the sensor was unstrained while various objects were brought to its vicinity, show that sensor's signal may be varied due to capacitive and inductive variation Figure 4.15. Therefore, during operation, sufficient attention must be paid to avoid signal variation which might be originated in capacitive (human skin [74]) as well as inductive effects. It may be possible to differentiate the capacitive effects from inductive ones, by utilizing a more sophisticated LC data acquisition unit capable of tracking capacitive and inductive effects independently.

The performance of sensors in these controlled tests enabled us to understand the basic characteristics and compare metrics between sensors with different mechanisms of sensing. Once installed in a device, performance with respect to tracking random movements—or more accurately strain—is not as straightforward. Subjecting the sensor to a random wave-form within its intended working range can give an indication of the accuracy for kinematic tracking. A random wave-form was produced with a maximum strain rate of 4.6%/s (5mm/s) within a strain range of 0-6%. The inductive sensor was able to accurately track strain with a NRMSE of 2.43% (Figure 4.12). This test was limited in its strain rate and in comparison, to the motion capture data of the intended application, we were aware that the actual frequency and strain rate required to track with our sensors for running was much higher—often upwards of 100 %/s (Figure 4.8)—with a stride frequency as high as 5 Hz for a sprinter [61], [62], [64], [76]. To analyze the ability of the sensor/device to track fast movements, the sensor was strained at frequencies from 0.1-20 Hz using a sine wave pattern (Figure 4.13 and Figure 4.14A). The sensor was still able to track minimum/maximum values effectively but exhibited an increasing lag with increasing frequency and strain rate above 4 Hz. The fastest human motion is around 10 Hz, typical of seizures which could be a suitable alternative application for these sensors [65] along with robotics applications that may require tracking strain at high frequencies/strain rates not capable in human motion.

Chapter 5.

Application of the Sensor Using Machine Learning for Multi-axis Kinematic Tracking

5.1. Introduction

The ability to track kinematics—complex body movements typically reserved for motion capture systems—with soft sensors has been growing with the development of both hardware (i.e. sensors, electronics, and wireless systems) and software (i.e. apps and neural networks) and has become increasingly accurate for complex movement [28], [30],[51]. Tracking lower body movements requires sensors to track at high frequency and speeds, upwards of 5 Hz for a sprinter gait [61], [62], [64], [76], although human body can move at a frequency beyond 10 Hz in certain circumstances such as seizures [65]. Higher frequencies can be difficult for common piezoresistive sensors to track because of the hysteresis and rate-dependent effects [47], [48], [66], whereas inductive sensors are not susceptible to these negative effects and theoretically should track fast frequency movement efficiently.

5.2. Experimental Setup

5.2.1. Smart sensor integrated sport short

A sensor-integrated tight-fitting sport shorts was developed to measure three-dimensional angles of the right hip. The prototype (**Error! Reference source not found.**B/C) was designed to measure hip joint kinematics during running by measuring multi-axial movements of the right hip joint by using 4 sensors, approximately 8 cm in length and a width of 4 cm for a total starting area of 32 cm^2. The locations and number of sensors chosen for this prototype were discussed earlier in section 4.4.

5.2.2. Experiment protocol and participants

To evaluate the performance of the prototype, 12 participants—2 females and 10 males—between the ages of 22-31 were recruited. The experimental protocol was approved by the Office of Research Ethics at Simon Fraser University. Prior to any data

collection, written informed consent was obtained from all participants (details of participants in **Error! Reference source not found.**)

The participant was asked to wear the tight-fitting prototype sport shorts and the optically trackable markers were affixed directly to the anatomical landmarks. After collecting the static calibration, each participant was asked to run at a speed of 2.0 m/s on a treadmill. This speed was chosen to ensure all participants could complete the entire testing protocol without breaks. The data collection for each participant involved one trial of 10 minutes of running, out of which, 9 minutes of data was used as training set for the random forest model and 1 minute as a test set.

Table 5.1 Participant's characteristics data.

Categories	Participants
Age (years)	25 (2.6)
Height (cm)	176 (8.6)
Weight (kg)	75 (10.25)

5.2.3. Experimental Setup and Reference Angle measurement

The method for obtaining the raw signal from the sensors has been explained in section 4.2. Six high-speed motion tracking cameras collected pelvis and right thigh kinematic data (and subsequently used as the standard for joint angles) from 8 retroreflective tracking markers using a modified lower extremity marker set [5]. Prior to dynamic trials, a static calibration trial was captured using an additional 6 static/calibration markers (Figure 5.1). This trial was used to construct the pelvis and right thigh model of each participant in Visual3D software.

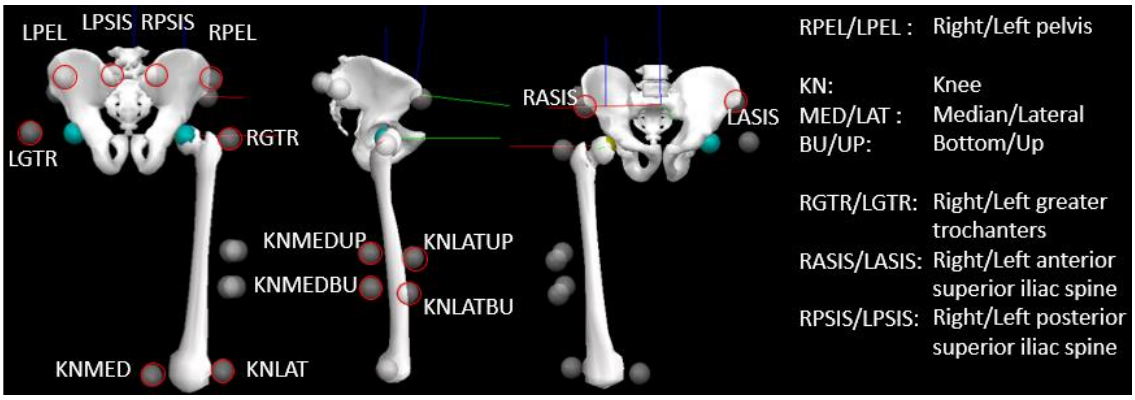

Figure 5.1. Anatomical landmarks on pelvis and hip for standard data to compare inductive sensor tracking obtained from Visual3D.

A signal from the motion tracking system was used to synchronize the sensors and motion capture data. Data from the sensors was collected at a frequency of 125 Hz and the motion tracking system at 100 Hz. The sensor data was interpolated and down sampled to the sampling rate of the motion tracking system (100 Hz) to match the number of samples in each trial.

The three-dimensional kinematic data was analyzed using Visual3D software and passed through a fourth-order Butterworth low-pass filter with a cut-off frequency of 6 Hz to remove high frequency noise. Reference angles were extracted from the filtered data. This filtering method is recommended in literature which have been applied when obtaining optical markers coordinates in an optical motion capturing systems [78],[40].

Accuracy of the reference angle measurement

To investigate the accuracy of a Vicon OMC system using standard laboratory equipment, a protocol was developed that provided results in terms of uncertainty and trueness of distance between two markers [24]. This protocol—carried out under setups using 6,8 and 10 cameras—targeted static and dynamic movements showing that number of cameras, height and movement conditions affected the accuracy [24]. In our study, 6 cameras were used which results in static uncertainty of less than 0.07 mm [24]. The static trueness of our measurement system could be up to 2.00, -0.56 and 0.79 mm for Z0 (0mm height), Z500 (500mm height) and Z1000 (1000mm height). Similarly, the uncertainty and trueness of two markers located around hip were found to be up to 3.28 mm and -0.90 mm.

According to another study. For calculating the position each reflective marker in a Vicon motion capture system, 1 mm of error is considered to be a standard [79]. Under this assumption, the calculation of the reference error for all collected data points lead to less than 2° in all three angles [80]. Due to the lack of a more accurate positioning system accessible during data collection, the kinematic measurements obtained from the Vicon motion capture system in this study, was assumed to be accurate while neglecting the error calculated in literature.

5.3. Data Analysis

5.3.1. Random Forest Regression

Background

According to literature [81], Random Forest regression is an ensemble of *K* trees$\{T_1(X), \dots, T_K(X)\}$, where $X = \{X_1, \dots, X_n\}$, is an *n*-dimensional vector of features associated with a molecule. The ensemble *K* outputs$\{\widehat{Y_1} = T_1(X), \dots, \widehat{Y_K} = T_K(X)\}$, where$\widehat{Y_1}, k = 1, \dots, K$, is the prediction for a molecule by the *k*th tree. Finally, all of the tree's outputs are accumulated to produce one final prediction $\hat{Y}$.

The training algorithm for a given training dataset *D* on a set of *m* molecules,$D = \{(X_1, Y_1), \dots, (X_m, Y_m)\}$, where $X_i, i = 1, \dots, m$, is a vector of features and $Y_i$is either the corresponding activity of interest (e.g., $-logIC_{50}$) is the following:

1. Drawing a bootstrap sample (i.e. randomly sample, with replacement, *m* molecules) from the training dataset of *m* molecules.
2. For each bootstrap sample, growing a tree with the following modification: at each node, choosing the best split among a randomly selected subset of j_{try} , rather than all descriptors, while the tree grows to the maximum size (i.e. until no further splits are possible) and not pruned back.
3. Repeating the above steps until (a sufficiently large number) *K* such trees are grown.

Similar to Decision Trees—which are known for their ability to select "important" features among many and ignore others [82]—Random Forest, as an ensemble of trees, has the ability to select "important" features. This is not produced as an explicit model, instead, the relationship between features and activity of interest is hidden inside a "black box" [83]. Nevertheless, an idea of each feature's importance in contribution to prediction accuracy is calculated during training and will be used later on to draw an analogy of which features are more important and why are they so, in this problem context.

5.3.2. Evaluation Metrics Definition

The performance of the joint angle measurement by the machine learning algorithm was assessed by comparing the predicted angle from the algorithm with the

reference angle measured by the motion capture system. The coefficient of determination (R^2), root mean squared error ($RMSE$), and the normalized root mean squared error ($NRMSE$) were used as metrics for comparison.

Using these metrics, we validated the performance of the machine-learning algorithm in an intra-participant analysis. In first evaluation approach, one separate model was trained and tested for each participant. A traditional ten-fold cross-validation method was used to evaluate the performance of the model. Each fold comprised all the movement conditions with the same speed. In this ten-fold cross-validation approach, the model was trained using the data from nine folds (equivalent to 9 minutes of running) and tested on the remaining fold (equivalent to 1 minute of running). This was repeated until all the ten folds were selected as the test set. The accuracy of the model was determined by averaging the results of all ten folds for each participant.

Because of the nature of the data which is time series, it is possible that traditional k-fold cross validation could cause data leakage and bias the performance [84]. Therefore, as a second evaluation approach, a 10-fold forward chaining method for training and testing each model were used. In this method, one separate model was trained and tested for each participant similar to the first approach, however instead of randomizing the test fold, the model was trained to predict only the future split. Using this technique, the data for a participant was split into 10 parts, then a separate model was trained using all possible consecutive splits while on future split was used for testing. For instance: 1) 1st split was used in training, 2nd in testing; 2) 1st and 2nd split in training, 3rd split in testing, etc. (Figure 5.2). The accuracy of the model was determined by averaging the results of all 9 validation splits for each participant. Additionally, in order to understand the effect of manual feature extraction which is discussed in the next section, the forward chaining evaluation technique was repeated once with and without manually extracted features in the dataset.

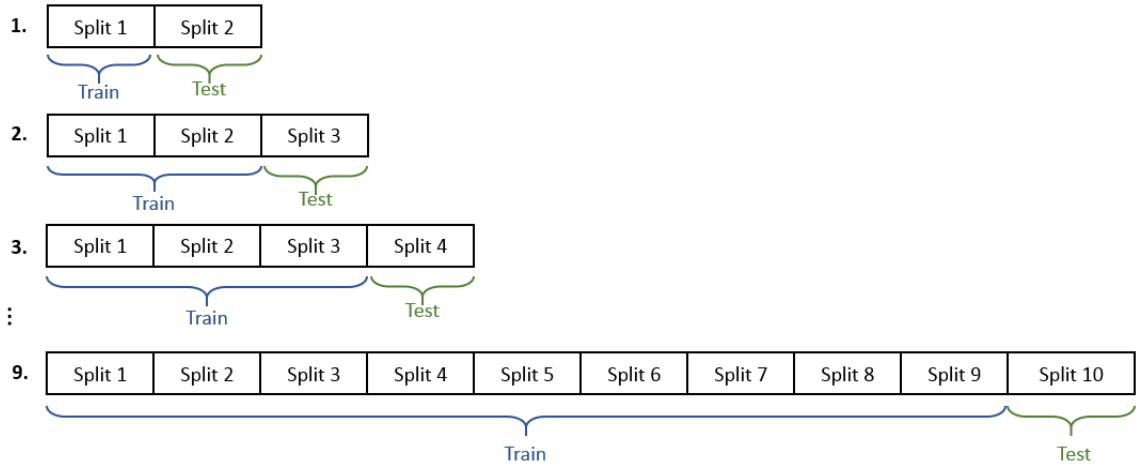

Figure 5.2. Forward chaining training and test splits in different sub-trial.

5.3.3. Feature extraction

Compared to Neural Network models—which are capable of automatically learning features [85]—Random Forest tries to educate the learners (ensemble of trees) with the given features [81]. In order to use a Random Forest model whose main task is to map raw signal of the four strain sensors (equally time-spaced) into the hip-joint angle in three dimensions, the input features were manually extracted for each trial (each participant).

To extract features useful for the Random Forest model, each pair of sensor signal values were numerically added together, deducted, divided by each other and multiplied by each other to extract inter-sensor features. The idea behind this method of feature extraction was to provide the model not only the values of sensors at each data point, but also their aggregation. For instance, during hip flexion (e.g. from 0 to 20 degrees) the frontal segments of the garment experience a negative strain while the area on the back of the garment is stretched. Therefore, the model could be benefited if the accumulation of each two possible sensors is provided.

Additionally, a 1st order derivative of each sensor's signal was added to the list of features. This enabled the model to be aware of strain rates applied to the sensors in addition to their absolute values, which the model could learn, how different strain rates can be related to a certain point in motion (e.g. foot strike).

Finally, a sliding window of 10 previous data points was added to the features to smooth the output signal. Using the aforementioned method, an input array size of [*n* x

720] was achieved for each participant, where *n* is the number of data points for each trial and 720 is the total number of features for each model.

Having 4 sensors:

- 16 (4 by 4) combination pairs were possible and using the four basic math operations between each pair of sensors (addition, deduction, multiplication and division) 64 features were obtained.
- 1st derivative of each sensor as well as four sensors raw signal (8 in total).
- A sliding window of 10 of each feature mentioned before.

It was possible to extract 720 (72x10) features from four sensors in each trial.

5.3.4. Application of Random Forest in Hip Joint Angle Estimation

Previously it was shown that strain on a garment can be correlated with body posture [45] and joint angle [46] using Machine Learning algorithms to learn the correlation given gold standard data. Random Forest was chosen to learn this correlation in a garment equipped with the inductive-based strain sensors and the results were validated using optoelectric motion capture output.

Random forest does not heavily depend on any individual feature, but instead, it aggregates ensembles predictions altogether [81]. This means that an ensemble can contribute more into an accurate prediction in one trail (one participant) while it might not be the case in another trial. Therefore, if not benefiting from such attribute, a model can perform accurately in one trial but not so well in another. This is beneficial when using the same garment for multiple participants whose strain to joint angle pattern is different from individual to another (e.g. due to weight, height, volume of body segments, etc).

In a Random Forest model, each tree brings in its own source and type of information in a whole picture. For instance, some trees, carry information about the range of motion while others care about which type of motion is happening (e.g. leg-swing). This enables the model to have access to a diversity of information as well as not allowing outliers to affect the overall performance of the model [86].

Random forest is a highly accurate algorithm among other top machine learning algorithms even without parameter tuning [81]. Number of estimators was chosen to be

1000 as well as true parameter for object out of bag score (OOB_score) and zero random state, while the rest of the hyper parameters were kept as default. Changing the number of estimators did not seem to affect the performance of the random forest model significantly, therefore no further hyper parameter tuning was attempted. The parameters used in all models were the same and are available in **Error! Reference source not found.**.

Table 5.2 List of chosen random forest parameters during.

Parameter name	Parameter description	Value
bootstrap	To use bootstrap of samples or not	True
criterion	Quality of a split measurement function	mse
max_features	Max number of features	auto
max_depth	Max depth of a tree	None
max_leaf_nodes	Max number of leaf nodes	None
min_impurity_decrease	Min for weighted impurity decrease	None
min_impurity_split	Threshold for early stopping	None
min_samples_leaf	Min number of samples to be leaf a node	1
min_samples_split	Min number for a split	2
min_weight_fraction_leaf	Min weighted fraction of the sum weights	0.0
n_estimators	The number of trees in the forst	1000
n_jobs	Number of jobs to run in parallel	-2
oob_score	To use out-of-bag samples or not	True
random_state	Controls randomness	0
warm_start	To fit a whole new forest or not	False
verbose	Controls the verbosity	0

5.4. Results

For each participant, ten-minutes of running data was collected. The random forest regressor estimated the sagittal plane (flexion/extension, Figure 5.3/A) angle of R^2 = 0.98 ± 0.01, RMSE = 1.63 ± 0.32°, and NRMSE = 3.45 ± 0.56%; the frontal plane (abduction/adduction, Figure 5.3/B) angle of R^2 = 0.93 ± 0.04, RMSE = 1.09 ± 0.22°, and NRMSE = 5.31 ± 0.96%; and the transverse plane (rotation Figure 5.3/C) angle with R^2 = 0.80 ± 0.09, RMSE = 1.17 ± 0.25°, and NRMSE = 7.35 ± 1.20% averaged over all participants in 10-fold cross validation. Among the three angles, the sagittal plane angle

estimation had the highest accuracy, while the transverse plane angle estimation had the lowest accuracy (Table 5.3 and Figure 5.3/A/B/C).

Table 5.3. Performance results of the algorithm in the estimation of three angles in sagittal (ψ), frontal (θ) and transverse (ϕ) planes, averaged across all participants, among three different training technique.

Plane	Evaluation metrics	10-fold cross validation with 720 features	10-split forward chaining with 40 features	10-split forward chaining with 720 features
Ψ	R^2	0.98(0.01)	0.97(0.01)	0.98(0.01)
	RMSE (Deg)	1.63(0.32)	2.12(0.31)	1.84(0.30)
	NRMSE (%)	3.45(0.56)	4.50(0.64)	3.99(0.64)
θ	R^2	0.93(0.04)	0.90(0.06)	0.92(0.05)
	RMSE (Deg)	1.09(0.22)	1.30(0.33)	1.16(0.3)
	NRMSE (%)	5.31(0.96)	6.53(1.36)	5.99(1.13)
ϕ	R^2	0.80(0.09)	0.76(0.14)	0.78(0.12)
	RMSE (Deg)	1.17(0.25)	1.32(0.29)	1.21(0.28)
	NRMSE (%)	7.35(1.2)	8.00(1.40)	7.52(1.39)

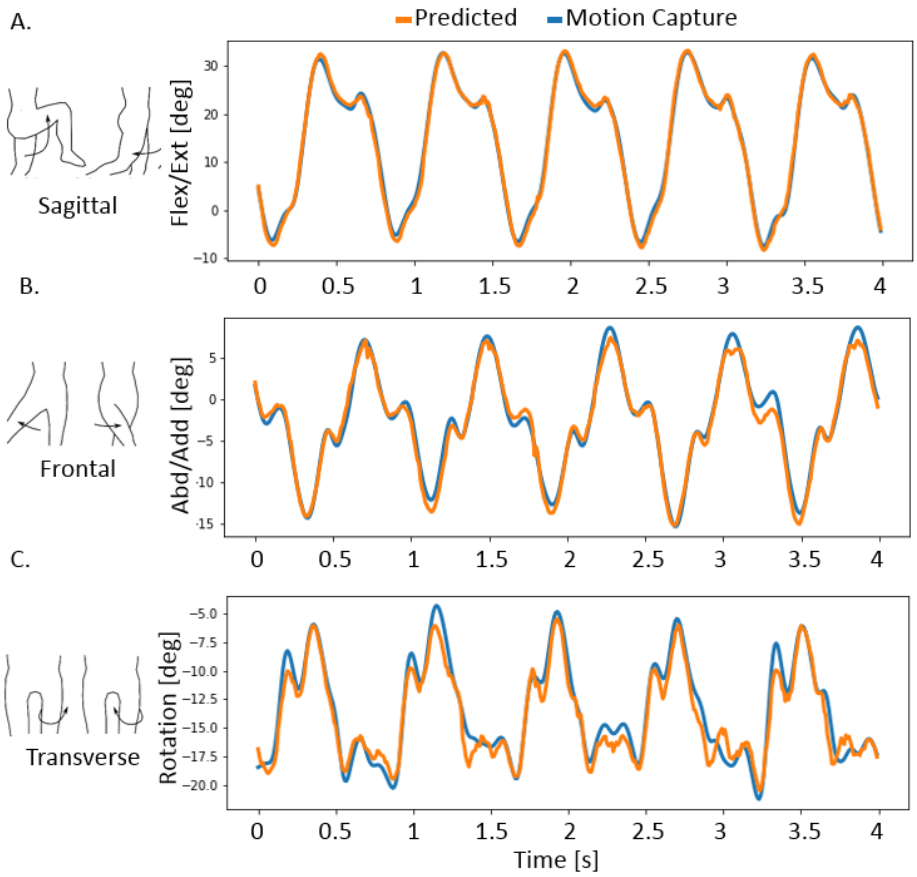

Figure 5.3. Comparison of kinematic tracking for different planes (depicted below each graph) during running. This includes: A) Flexion-Extension (sagittal plane); B) Abduction-Adduction (frontal plane); C) Rotation (transverse plane).

Top 11 features with respect to their importance assigned by a random forest model among one participant is presented in Figure 5.4. Since random forest does not extract features and instead works with the features provided as input, some features manually extracted such as addition, deduction, etc. between channels appeared to be very useful to the model. It can be seen that all manually extracted features, such as math operations, derivatives and past window were among 11 most important features.

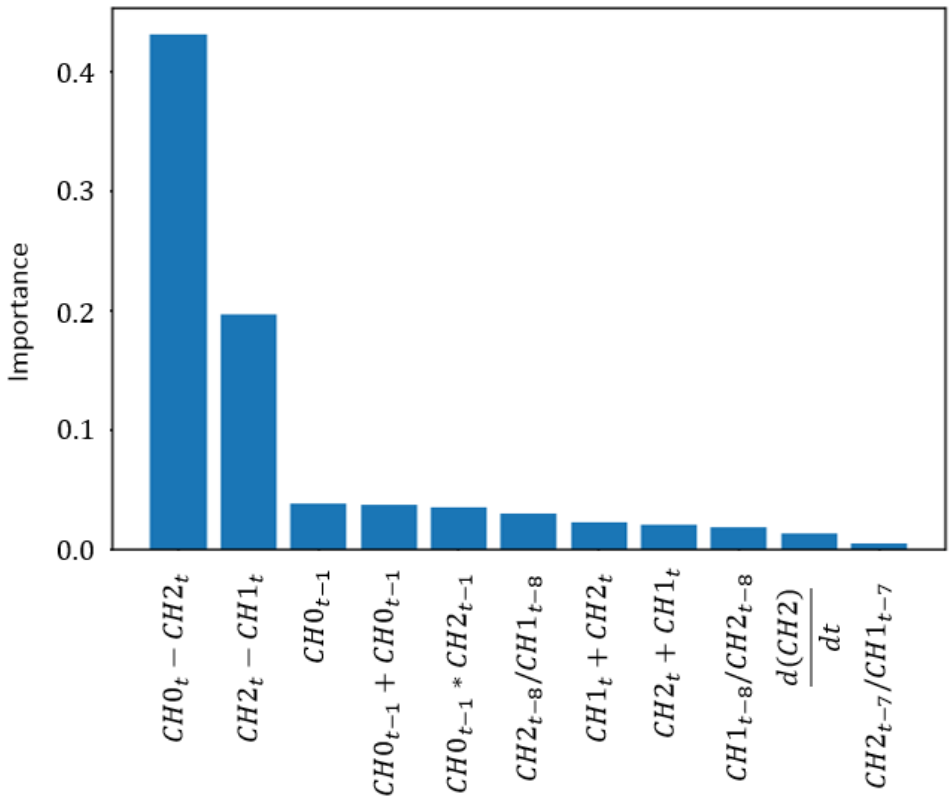

Figure 5.4. 11 most important features in a sample model. CHx represent sensor X raw data and subscript t represent the past window. e.g. $CH1_{t-8}$ means channel 1 raw data at 8th past window.

5.5. Discussion and Conclusion

The number of sensors used in the prototype was limited by the LDC1614 chip capability of reading four sensors simultaneously. The placements of the sensors had to enable each sensor to undergo strain during motions in different planes. Each sensor was placed in different orientations (horizontal/vertical/orthogonal, Figure 4.7/B/C) in order to allow the system to learn as many unique relationships between strain of each sensor and motions/angles in different planes (sagittal, frontal, transverse).

Stretchable fabrics may vary in elasticity as a result of different ratio of stretchable and non-stretchable material used during production. There were two types of fabrics used in this system: the sensor's core material which was a commercially available elastic thread and the fabric on which the loops were attached to. Different amount of elasticity between the two types of fabrics may cause the sensor to undergo strain at a higher (if both are highly elastic) or lower (if one is less elastic) strain rate and strain %. In order to

demonstrate the sensor's performance during the cohort test, it was stretched up to the highest possible (with available technology) strain rate and maximum strain % each sensor experienced during 2-minutes of running. These tests illustrated the sensor performance in higher (i.e. due to higher elasticity) and lower (i.e. due to lower elasticity) strain rate as well as strain %.

The smart compression shorts fabricated in this work captured motion in three dimensions during a moderate speed of running at 2.0 m/s. To our knowledge, there have been no previous reports of quantitative tracking of lower body motion using inductive sensors and only one classification-based motion tracking and one regression-based single-axis angular motion [21], [23]. Running speeds are variable and that while this pace was slower than average, it was what our participants could manage comfortably. It was important for our participants to run at a speed that allowed them to maintain their normal running mechanics. We expect the shorts to perform equally well at higher running speeds (upwards of 5 Hz for a sprinter) because the inductive sensors are not susceptible to negative effects such as hysteresis and rate-dependent effects (as in piezoelectric sensors) and therefore should track fast frequency movement efficiently. Thus, we do not feel that it is necessary to evaluate the effect of faster running on tracking accuracy as even sprinting is under the threshold of frequency that our inductive sensor can measure.

While Random Forest is known to be data-driven statistical method [87], they exhibit to be consistent [88]–[90], reduce variance while not increasing the prediction bias [91], reach minmax rate of convergence while adapting to sparsity [92], [93]. Random Forest regressor was chosen as a machine learning model candidate to be trained and tested for estimation of joint angle using only strain sensors raw data. Other machine learning models such as Convolutional Neural Network (CNN) and Long-Short term Memory networks (LSTM) have been tried, however in addition to extra time and computing requirements of such models, compared with Random Forest, advanced efforts for hyper-parameter optimization as well as model-specifications selections were required to achieve a sufficient accuracy. The mentioned Deep-Learning algorithms were tested1 while their accuracy did not outweigh that of the random forest regressor, which are considered to be highly accurate even without extensive hyper-parameter selections [81].

Hip angles were estimated with an RMSE of less than 1.63°, 1.09°, and 1.17° in the sagittal, frontal and transverse planes, respectively. The performance results were

averaged among all participants during the activity. The random forest regressor was able to provide excellent estimation in the sagittal plane (R^2=0.98) and in frontal plane ($\boldsymbol{R^2}$=0.93) but the accuracy was decreased in the transverse plane (R^2=0.80). The larger range of motion in the sagittal and frontal planes (45° and 15°, respectively) compared to the transverse plane (5°) [94]**,** results in larger relative error (~1° of 5° for the transverse plane) and reduces accuracy as a direct result of the smaller range of motion. Additionally, the kinematic profile of the transverse plane joint angle of the hip is a more complicated pattern during running [94] in comparison to the sagittal plane and frontal plane. Further improvement of this accuracy would require the use of more sensors with high sensitivity to the transverse movement. Furthermore, while optical motion capture technology is considered the gold standard approach to measuring running biomechanics [95] , it is also less accurate in the transverse plane compared to sagittal or frontal tracking [96], and may be a source of error in our results [94].

In order to understand the temporal order inherent in the participant's data, instead of traditional 10-fold cross-validation, 10-fold forward chaining technique was used during training and testing. The results showed that RMSE and NRMSE changed no more than 0.21° and 0.68% respectively, which showed that there was no significant difference in accuracy obtained using traditional k-fold cross-validation technique, compared with forward chaining technique, using all 720 features extracted.

To understand the effect of including numerically modified signal values, such as addition, subtraction, first order derivative of each signal, etc., every participant's data was used to train another model only using raw signal and a window of 10 past data points. Comparing the results of the two sets of features (one using all 720 features and another one using only 40=4x10 features) using forward chaining, R2 score of sagittal and frontal and transverse estimation improved by less than 2% after including the additional features. Despite RMSE did not improve more than 0.72° among all planes, NRMSE improved by 0.54% for frontal and transverse plane.

Placement of additional sensors to improve the sensor signals would likely lead to improved accuracy, although it is important to note that avoiding areas that wrinkle during the stride to reduce any false signals that could contribute to error. Noise introduced into the signal as a result of foot-strikes—which typically involve shocks and vibrations to the sensors from ground-force impact [97]—can be reduced by tighter, more form fitting

garments for each participant. It is significant to note that sweat did not adversely affect the inductive sensors performance, an aspect that is typically problematic for piezoresistive and capacitive sensors in wet environments and require an insulting coating/sheath for protection [43]. Furthermore, temperature and moisture are not expected to affect the performance of the sensors, although further testing is required to ensure feasibility in different working environments and washability.

Chapter 6.

Conclusion

In this work, after studying previously developed soft strain sensors and basic requirements, a novel inductive-based strain sensor which required no chemical process was fabricated. It was possible to derive two formulae which verified the inductance-strain correlation under the given sensor configuration. Due to assumption and approximation taken when applying the formulae, none of these formulae were capable of accurately calculating the sensor's signal upon a change in sensor's length and the gauge factor, however the gauge factor obtained after normalizing the signals were in agreements with both formulae's results.

Attributes such as sensor's signal stability over static and dynamic tests were studied by conducting various tensile tests. It was found that the fabricated sensor was capable of tracking high strain rates—it is not often obtainable by resistive-based and capacitive-based strain sensors [14], [48]. The sensor showed a sufficient signal stability under static and dynamic tests which suggests that this technology can be utilized for various purposes requiring high and low speed, after considering the electromagnetic sensitivity of the sensor in different environment setups.

The sensor was stretched up to 100% and the sensor behavior (strain vs inductance) was observed to be the similar compared to 30% strain test. However advanced tests such as cyclic test, hysteresis etc were not carried out again for a range of up to 100% because the range of operation in terms of strain % and strain rate in the intended cohort test was found to be a maximum of 30%. It is worth noting that strain sensors do not necessarily need to be used right at the joint areas where maximum strain happens but can be deployed at any area at vicinity of the joint as long as some level of strain exist in the garment and can be measured by the sensor.

Overall, our developed smart compression shorts system was able to track multi-axial thigh movements with respect to pelvis during running in three dimensions with errors less than 1.63**°.** Inductive sensors show very little drift, the ability to capture motion at a high strain rate (453%/s) and frequency (20 Hz) without any discernable hysteresis. This shows the great potential for inductive–based sensor smart textile systems to provide

feedback useful for injury prevention, performance tracking and enhancement, or robotics [7], [17], [59], [97]–[99]. Furthermore, the sensors can be produced in different geometries to optimize signal-to-noise and stability, and behavior would be predictable using theoretical formulas that describe the signal. This method would enable immediate integration into textiles and garments available commercially.

In conclusion, it is worth noting that although strain sensors may not seem to be outperforming other motion capturing systems such as OMC and EMS, their compactness, comfortability and sufficient accuracy can justify the need for further developments and deployment into the proper markets such as sport and personal training.

References

[1] P. T. Nikolaidis, I. Cuk, T. Rosemann, and B. Knechtle, “Performance and Pacing of Age Groups in Half-Marathon and Marathon,” *IJERPH*, vol. 16, no. 10, p. 1777, May 2019, doi: 10.3390/ijerph16101777.

[2] M. Van Middelkoop, J. Kolkman, J. Van Ochten, S. M. A. Bierma-Zeinstra, and B. W. Koes, “Risk factors for lower extremity injuries among male marathon runners,” *Scand J Med Sci Sports*, vol. 18, no. 6, pp. 691–697, Dec. 2008, doi: 10.1111/j.1600-0838.2007.00768.x.

[3] H. Tanaka and D. R. Seals, “Endurance exercise performance in Masters athletes: age-associated changes and underlying physiological mechanisms,” *J. Physiol. (Lond.)*, vol. 586, no. 1, pp. 55–63, Jan. 2008, doi: 10.1113/jphysiol.2007.141879.

[4] K. B. Fields, J. C. Sykes, K. M. Walker, and J. C. Jackson, “Prevention of running injuries,” *Curr Sports Med Rep*, vol. 9, no. 3, pp. 176–182, Jun. 2010, doi: 10.1249/JSR.0b013e3181de7ec5.

[5] C. Napier, C. L. MacLean, J. Maurer, J. E. Taunton, and M. A. Hunt, “Kinetic risk factors of running-related injuries in female recreational runners,” *Scandinavian Journal of Medicine & Science in Sports*, vol. 28, no. 10, pp. 2164–2172, 2018, doi: 10.1111/sms.13228.

[6] S. Willwacher, M. Sanno, and G.-P. Brüggemann, “Fatigue matters: An intense 10 km run alters frontal and transverse plane joint kinematics in competitive and recreational adult runners,” *Gait & Posture*, Dec. 2019, doi: 10.1016/j.gaitpost.2019.11.016.

[7] C. Napier, C. L. MacLean, J. Maurer, J. E. Taunton, and M. A. Hunt, “Real-Time Biofeedback of Performance to Reduce Braking Forces Associated With Running-Related Injury: An Exploratory Study,” *J Orthop Sports Phys Ther*, vol. 49, no. 3, pp. 136–144, Mar. 2019, doi: 10.2519/jospt.2019.8587.

[8] M. Stoppa and A. Chiolerio, “Wearable Electronics and Smart Textiles: A Critical Review,” *Sensors (Basel)*, vol. 14, no. 7, pp. 11957–11992, Jul. 2014, doi: 10.3390/s140711957.

[9] M. Kaisti *et al.*, “Clinical assessment of a non-invasive wearable MEMS pressure sensor array for monitoring of arterial pulse waveform, heart rate and detection of atrial fibrillation,” *npj Digit. Med.*, vol. 2, no. 1, pp. 1–10, May 2019, doi: 10.1038/s41746-019-0117-x.

[10] V. Toral *et al.*, “Wearable System for Biosignal Acquisition and Monitoring Based on Reconfigurable Technologies,” *Sensors (Basel)*, vol. 19, no. 7, Apr. 2019, doi: 10.3390/s19071590.

[11] S. Imani *et al.*, “A wearable chemical–electrophysiological hybrid biosensing system for real-time health and fitness monitoring,” *Nat Commun*, vol. 7, no. 1, pp. 1–7, May 2016, doi: 10.1038/ncomms11650.

[12] F. Yin *et al.*, “Highly Sensitive and Transparent Strain Sensors with an Ordered Array Structure of AgNWs for Wearable Motion and Health Monitoring,” *Sci Rep*, vol. 9, no. 1, pp. 1–10, Feb. 2019, doi: 10.1038/s41598-019-38931-x.

[13] D. R. Seshadri *et al.*, “Wearable sensors for monitoring the internal and external workload of the athlete,” *npj Digit. Med.*, vol. 2, no. 1, pp. 1–18, Jul. 2019, doi: 10.1038/s41746-019-0149-2.

[14] M. Amjadi, Y. J. Yoon, and I. Park, “Ultra-stretchable and skin-mountable strain sensors using carbon nanotubes–Ecoflex nanocomposites,” *Nanotechnology*, vol. 26, no. 37, p. 375501, Aug. 2015, doi: 10.1088/0957-4484/26/37/375501.

[15] Jianguo Zhang, Haiyan Song, and Qiang Xue, “Study on motion measurement of human upper limb based on electromagnetic tracking system,” in *2008 IEEE International Conference on Industrial Engineering and Engineering Management*, 2008, pp. 768–771, doi: 10.1109/IEEM.2008.4737973.
[16] R. Needham, J. Stebbins, and N. Chockalingam, “Three-dimensional kinematics of the lumbar spine during gait using marker-based systems: a systematic review,” *Journal of Medical Engineering & Technology*, vol. 40, no. 4, pp. 172–185, May 2016, doi: 10.3109/03091902.2016.1154616.
[17] J. P. Folland, S. J. Allen, M. I. Black, J. C. Handsaker, and S. E. Forrester, “Running Technique is an Important Component of Running Economy and Performance,” *Med Sci Sports Exerc*, vol. 49, no. 7, pp. 1412–1423, 2017, doi: 10.1249/MSS.0000000000001245.
[18] L. Chiari, U. D. Croce, A. Leardini, and A. Cappozzo, “Human movement analysis using stereophotogrammetry. Part 2: Instrumental errors,” *Gait & posture*, vol. 21, no. 2, pp. 197–211, Feb. 2005, doi: 10.1016/j.gaitpost.2004.04.004.
[19] U. Della Croce, A. Leardini, L. Chiari, and A. Cappozzo, “Human movement analysis using stereophotogrammetry: Part 4: assessment of anatomical landmark misplacement and its effects on joint kinematics,” *Gait & Posture*, vol. 21, no. 2, pp. 226–237, Feb. 2005, doi: 10.1016/j.gaitpost.2004.05.003.
[20] A. Leardini, L. Chiari, U. C. Della, and A. Cappozzo, “Human movement analysis using stereophotogrammetry. Part 3. Soft tissue artifact assessment and compensation.,” *Gait Posture*, vol. 21, no. 2, pp. 212–225, Feb. 2005, doi: 10.1016/j.gaitpost.2004.05.002.
[21] R. Wijesiriwardana, “Inductive fiber-meshed strain and displacement transducers for respiratory measuring systems and motion capturing systems,” *IEEE Sensors Journal*, vol. 6, no. 3, pp. 571–579, Jun. 2006, doi: 10.1109/JSEN.2006.874488.
[22] L. Chen *et al.*, “Whole System Design of a Wearable Magnetic Induction Sensor for Physical Rehabilitation,” *Advanced Intelligent Systems*, vol. 1, no. 2, p. 1900037, 2019, doi: 10.1002/aisy.201900037.
[23] B. Bonroy, K. Meijer, P. Dunias, K. Cuppens, R. Gransier, and B. Vanrumste, “Ambulatory Monitoring of Physical Activity Based on Knee Flexion/Extension Measured by Inductive Sensor Technology,” *ISRN Biomedical Engineering*, vol. 2013, no. 908452, 2013, doi: 10.1155/2013/908452.
[24] P. Eichelberger *et al.*, “Analysis of accuracy in optical motion capture – A protocol for laboratory setup evaluation,” *Journal of Biomechanics*, vol. 49, no. 10, pp. 2085–2088, Jul. 2016, doi: 10.1016/j.jbiomech.2016.05.007.
[25] M. Sakaguchi, H. Ogawa, N. Shimizu, H. Kanehisa, T. Yanai, and Y. Kawakami, “Gender differences in hip and ankle joint kinematics on knee abduction during running,” *European Journal of Sport Science*, vol. 14, no. sup1, pp. S302–S309, Jan. 2014, doi: 10.1080/17461391.2012.693953.
[26] E. van der Kruk and M. M. Reijne, “Accuracy of human motion capture systems for sport applications; state-of-the-art review,” *European Journal of Sport Science*, vol. 18, no. 6, pp. 806–819, Jul. 2018, doi: 10.1080/17461391.2018.1463397.
[27] D. Zhong and S.-F. Chang, “Real-time View Recognition and Event Detection for Sports Video,” *J. Vis. Comun. Image Represent.*, vol. 15, no. 3, pp. 330–347, Sep. 2004, doi: 10.1016/j.jvcir.2004.04.009.
[28] A. Shingade and A. Ghotkar, “Animation of 3D Human Model Using Markerless Motion Capture Applied To Sports,” *IJCGA*, vol. 4, no. 1, pp. 27–39, Jan. 2014, doi: 10.5121/ijcga.2014.4103.
[29] E. Lluna, V. Santiago, B. Defez, L. Dunai, and G. Peris-Fajarnes, “Velocity vector (3D) measurement for spherical objects using an electro-optical device,”

Measurement, vol. 44, no. 9, pp. 1723–1729, Nov. 2011, doi: 10.1016/j.measurement.2011.07.006.
[30] X. Robert-Lachaine, H. Mecheri, C. Larue, and A. Plamondon, “Validation of inertial measurement units with an optoelectronic system for whole-body motion analysis,” *Med Biol Eng Comput*, vol. 55, no. 4, pp. 609–619, Apr. 2017, doi: 10.1007/s11517-016-1537-2.
[31] T.-H. Ha, K. Saber-Sheikh, A. P. Moore, and M. P. Jones, “Measurement of lumbar spine range of movement and coupled motion using inertial sensors - a protocol validity study,” *Man Ther*, vol. 18, no. 1, pp. 87–91, Feb. 2013, doi: 10.1016/j.math.2012.04.003.
[32] W. Teufl, M. Miezal, B. Taetz, M. Fröhlich, and G. Bleser, “Validity of inertial sensor based 3D joint kinematics of static and dynamic sport and physiotherapy specific movements,” *PLOS ONE*, vol. 14, no. 2, p. e0213064, Feb. 2019, doi: 10.1371/journal.pone.0213064.
[33] A. Leardini, Z. Sawacha, G. Paolini, S. Ingrosso, R. Nativo, and M. G. Benedetti, “A new anatomically based protocol for gait analysis in children,” *Gait Posture*, vol. 26, no. 4, pp. 560–571, Oct. 2007, doi: 10.1016/j.gaitpost.2006.12.018.
[34] W. Teufl, “Joint angle calculation from optical markers and IMUs attached to the lower body,” Feb. 2019, doi: 10.17504/protocols.io.vwye7fw.
[35] “A Review on Wearable Inertial Tracking based Human Gait Analysis and Control Strategies of Lower-Limb Exoskeletons,” *International Robotics & Automation Journal*, vol. Volume 3, no. Issue 7, Dec. 2017, doi: 10.15406/iratj.2017.03.00080.
[36] T. Hiller, Z. Pentek, J.-T. Liewald, A. Buhmann, and H. Roth, “Origins and Mechanisms of Bias Instability Noise in a Three-Axis Mode-Matched MEMS Gyroscope,” *Journal of Microelectromechanical Systems*, vol. 28, no. 4, pp. 586–596, Aug. 2019, doi: 10.1109/JMEMS.2019.2921607.
[37] A. Ancillao, S. Tedesco, J. Barton, and B. O’Flynn, “Indirect Measurement of Ground Reaction Forces and Moments by Means of Wearable Inertial Sensors: A Systematic Review,” *Sensors (Basel)*, vol. 18, no. 8, Aug. 2018, doi: 10.3390/s18082564.
[38] P. Picerno, “25 years of lower limb joint kinematics by using inertial and magnetic sensors: A review of methodological approaches,” *Gait Posture*, vol. 51, pp. 239–246, 2017, doi: 10.1016/j.gaitpost.2016.11.008.
[39] “Gyro Mechanical Performance: The Most Important Parameter | Analog Devices.” [Online]. Available: https://www.analog.com/en/technical-articles/gyro-mechanical-performance.html#. [Accessed: 21-Dec-2019].
[40] J.-T. Zhang, A. C. Novak, B. Brouwer, and Q. Li, “Concurrent validation of Xsens MVN measurement of lower limb joint angular kinematics,” *Physiol Meas*, vol. 34, no. 8, pp. N63-69, Aug. 2013, doi: 10.1088/0967-3334/34/8/N63.
[41] M. Gholami, A. Ejupi, A. Rezaei, A. Ferrone, and C. Menon, “Estimation of Knee Joint Angle Using a Fabric-Based Strain Sensor and Machine Learning: A Preliminary Investigation,” in *2018 7th IEEE International Conference on Biomedical Robotics and Biomechatronics (Biorob)*, 2018, pp. 589–594, doi: 10.1109/BIOROB.2018.8487199.
[42] J. H. M. Bergmann, S. Anastasova-Ivanova, I. Spulber, V. Gulati, P. Georgiou, and A. McGregor, “An Attachable Clothing Sensor System for Measuring Knee Joint Angles,” *IEEE Sensors Journal*, vol. 13, no. 10, pp. 4090–4097, Oct. 2013, doi: 10.1109/JSEN.2013.2277697.
[43] “Wearable soft sensing suit for human gait measurement - Yiğit Mengüç, Yong-Lae Park, Hao Pei, Daniel Vogt, Patrick M. Aubin, Ethan Winchell, Lowell Fluke, Leia Stirling, Robert J. Wood, Conor J. Walsh, 2014.” [Online]. Available:

https://journals-sagepub-com.proxy.lib.sfu.ca/doi/full/10.1177/0278364914543793. [Accessed: 28-Nov-2019].
[44] A. Rezaei, T. J. Cuthbert, M. Gholami, and C. Menon, “Application-Based Production and Testing of a Core–Sheath Fiber Strain Sensor for Wearable Electronics: Feasibility Study of Using the Sensors in Measuring Tri-Axial Trunk Motion Angles,” *Sensors*, vol. 19, no. 19, p. 4288, Jan. 2019, doi: 10.3390/s19194288.
[45] C. Mattmann, “Body posture detection using strain sensitive clothing,” 2008, doi: 10.3929/ethz-a-005698162.
[46] C. Mattmann, O. Amft, H. Harms, G. Troster, and F. Clemens, “Recognizing Upper Body Postures using Textile Strain Sensors,” in *2007 11th IEEE International Symposium on Wearable Computers*, 2007, pp. 29–36, doi: 10.1109/ISWC.2007.4373773.
[47] M. Gholami, A. Rezaei, T. J. Cuthbert, C. Napier, and C. Menon, “Lower Body Kinematics Monitoring in Running Using Fabric-Based Wearable Sensors and Deep Convolutional Neural Networks,” *Sensors*, vol. 19, no. 23, p. 5325, Jan. 2019, doi: 10.3390/s19235325.
[48] J.-S. Kim and G.-W. Kim, “Hysteresis Compensation of Piezoresistive Carbon Nanotube/Polydimethylsiloxane Composite-Based Force Sensors,” *Sensors*, vol. 17, no. 2, p. 229, Feb. 2017, doi: 10.3390/s17020229.
[49] A. Oliveri, M. Maselli, M. Lodi, M. Storace, and M. Cianchetti, “Model-Based Compensation of Rate-Dependent Hysteresis in a Piezoresistive Strain Sensor,” *IEEE Transactions on Industrial Electronics*, vol. 66, no. 10, pp. 8205–8213, Oct. 2019, doi: 10.1109/TIE.2018.2884204.
[50] S. Seyedin *et al.*, “Textile strain sensors: a review of the fabrication technologies, performance evaluation and applications,” *Mater. Horiz.*, vol. 6, no. 2, pp. 219–249, Feb. 2019, doi: 10.1039/C8MH01062E.
[51] Z. F. Liu *et al.*, “Hierarchically buckled sheath-core fibers for superelastic electronics, sensors, and muscles,” *Science*, vol. 349, no. 6246, pp. 400–404, Jul. 2015, doi: 10.1126/science.aaa7952.
[52] O. Atalay and W. R. Kennon, “Knitted strain sensors: impact of design parameters on sensing properties,” *Sensors (Basel)*, vol. 14, no. 3, pp. 4712–4730, Mar. 2014, doi: 10.3390/s140304712.
[53] G. Keulemans, P. Pelgrims, M. Bakula, F. Ceyssens, and R. Puers, “An Ionic Liquid Based Strain Sensor for Large Displacements,” *Procedia Engineering*, vol. 87, pp. 1123–1126, Jan. 2014, doi: 10.1016/j.proeng.2014.11.362.
[54] C. B. Cooper *et al.*, “Stretchable Capacitive Sensors of Torsion, Strain, and Touch Using Double Helix Liquid Metal Fibers,” *Advanced Functional Materials*, vol. 27, no. 20, p. 1605630, 2017, doi: 10.1002/adfm.201605630.
[55] L. Cai *et al.*, “Super-stretchable, Transparent Carbon Nanotube-Based Capacitive Strain Sensors for Human Motion Detection,” *Scientific Reports*, vol. 3, p. 3048, Oct. 2013, doi: 10.1038/srep03048.
[56] A. Frutiger *et al.*, “Capacitive Soft Strain Sensors via Multicore–Shell Fiber Printing,” *Advanced Materials*, vol. 27, no. 15, pp. 2440–2446, 2015, doi: 10.1002/adma.201500072.
[57] Y. Mengüç *et al.*, “Wearable soft sensing suit for human gait measurement,” *The International Journal of Robotics Research*, vol. 33, no. 14, pp. 1748–1764, Dec. 2014, doi: 10.1177/0278364914543793.
[58] E. Sardini, M. Serpelloni, and M. Ometto, “Smart vest for posture monitoring in rehabilitation exercises,” in *2012 IEEE Sensors Applications Symposium Proceedings*, 2012, pp. 1–5, doi: 10.1109/SAS.2012.6166300.

[59] Y. Huang *et al.*, “Self-similar design for stretchable wireless LC strain sensors,” *Sensors and Actuators A: Physical*, vol. 224, pp. 36–42, Apr. 2015, doi: 10.1016/j.sna.2015.01.004.
[60] T. G. Thuruthel, B. Shih, C. Laschi, and M. T. Tolley, “Soft robot perception using embedded soft sensors and recurrent neural networks,” *Science Robotics*, vol. 4, no. 26, Jan. 2019, doi: 10.1126/scirobotics.aav1488.
[61] K. J. Lee, N. Chou, and S. Kim, “A Batteryless, Wireless Strain Sensor Using Resonant Frequency Modulation,” *Sensors (Basel)*, vol. 18, no. 11, Nov. 2018, doi: 10.3390/s18113955.
[62] C. T. Farley and O. González, “Leg stiffness and stride frequency in human running,” *Journal of Biomechanics*, vol. 29, no. 2, pp. 181–186, Feb. 1996, doi: 10.1016/0021-9290(95)00029-1.
[63] A. Monte, V. Muollo, F. Nardello, and P. Zamparo, “Sprint running: how changes in step frequency affect running mechanics and leg spring behaviour at maximal speed,” *Journal of Sports Sciences*, vol. 35, no. 4, pp. 339–345, Feb. 2017, doi: 10.1080/02640414.2016.1164336.
[64] M. Paruzel-Dyja, A. Walaszczyk, and J. Iskra, “Elite male and female sprinters’ body build, stride length and stride frequency,” *Studies in Physical Culture & Tourism*, vol. 13, Nov. 1, 2006, 2006.
[65] G. P. Paradisis, A. Bissas, P. Pappas, E. Zacharogiannis, A. Theodorou, and O. Girard, “Sprint mechanical differences at maximal running speed: Effects of performance level,” *Journal of Sports Sciences*, vol. 37, no. 17, pp. 2026–2036, Sep. 2019, doi: 10.1080/02640414.2019.1616958.
[66] M. Velez, R. S. Fisher, V. Bartlett, and S. Le, “Tracking generalized tonic-clonic seizures with a wrist accelerometer linked to an online database,” *Seizure*, vol. 39, pp. 13–18, Jul. 2016, doi: 10.1016/j.seizure.2016.04.009.
[67] Y. Li, Y. A. Samad, T. Taha, G. Cai, S.-Y. Fu, and K. Liao, “Highly Flexible Strain Sensor from Tissue Paper for Wearable Electronics,” *ACS Sustainable Chem. Eng.*, vol. 4, no. 8, pp. 4288–4295, Aug. 2016, doi: 10.1021/acssuschemeng.6b00783.
[68] S. Tatsumi, Y. Yuuki, and H. Makino, “Elastic signal transmission cable,” US8969724B2, 03-Mar-2015.
[69] V. G. Welsby, *The theory and design of inductance coils*. Macdonald, 1950.
[70] S.-Y. Wu and W. Hsu, “Design and characterization of LC strain sensors with novel inductor for sensitivity enhancement,” *Smart Mater. Struct.*, vol. 22, no. 10, p. 105015, Sep. 2013, doi: 10.1088/0964-1726/22/10/105015.
[71] L. F. Shatz and C. W. Christensen, “Numerical Inductance Calculations Based on First Principles,” *PLoS One*, vol. 9, no. 11, Nov. 2014, doi: 10.1371/journal.pone.0111643.
[72] F. W. Grover, *Inductance Calculations: Working Formulas and Tables*. Dover Publications, Inc, New York, 1946.
[73] P. N. Murgatroyd, “The Brooks inductor: a study of optimal solenoid cross-sections,” *IEE Proceedings B - Electric Power Applications*, vol. 133, no. 5, pp. 309–314, Nov. 1986, doi: 10.1049/ip-b.1986.0041.
[74] D. T. N. Chen, Q. Wen, P. A. Janmey, J. C. Crocker, and A. G. Yodh, “Rheology of Soft Materials,” *Annual Review of Condensed Matter Physics*, vol. 1, no. 1, pp. 301–322, 2010, doi: 10.1146/annurev-conmatphys-070909-104120.
[75] H. Elfekey, H. A. Bastawrous, and S. Okamoto, “A Touch Sensing Technique Using the Effects of Extremely Low Frequency Fields on the Human Body,” *Sensors (Basel)*, vol. 16, no. 12, Dec. 2016, doi: 10.3390/s16122049.

[76] J. Park, I. You, S. Shin, and U. Jeong, “Material Approaches to Stretchable Strain Sensors,” *ChemPhysChem*, vol. 16, no. 6, pp. 1155–1163, 2015, doi: 10.1002/cphc.201402810.
[77] A. I. Salo, I. N. Bezodis, A. M. Batterham, and D. G. Kerwin, “Elite Sprinting,” in *Medicine & science in sports & exercise.*, 2011, vol. 43, pp. 1055–1062, doi: 10.1249/MSS.0b013e318201f6f8.
[78] D. Kim, J. Kwon, S. Han, Y.-L. Park, and S. Jo, “Deep Full-Body Motion Network for a Soft Wearable Motion Sensing Suit,” *IEEE/ASME Transactions on Mechatronics*, vol. 24, no. 1, pp. 56–66, Feb. 2019, doi: 10.1109/TMECH.2018.2874647.
[79] R. A. Bogey, A. J. Gitter, and L. A. Barnes, “Determination of ankle muscle power in normal gait using an EMG-to-force processing approach,” *Journal of Electromyography and Kinesiology*, vol. 20, no. 1, pp. 46–54, Feb. 2010, doi: 10.1016/j.jelekin.2008.09.013.
[80] P. Merriaux, Y. Dupuis, R. Boutteau, P. Vasseur, and X. Savatier, “A Study of Vicon System Positioning Performance,” *Sensors (Basel)*, vol. 17, no. 7, Jul. 2017, doi: 10.3390/s17071591.
[81] A. Rezaei, “Towards Wearable Platform for Accurate Unconstrained Trunk Motion Tracking Using Inertial and Strain Sensors Data Fusion,” p. 85.
[82] V. Svetnik, A. Liaw, C. Tong, J. C. Culberson, R. P. Sheridan, and B. P. Feuston, “Random Forest: A Classification and Regression Tool for Compound Classification and QSAR Modeling,” *J. Chem. Inf. Comput. Sci.*, vol. 43, no. 6, pp. 1947–1958, Nov. 2003, doi: 10.1021/ci034160g.
[83] A. A. Freitas, K. Limbu, and T. Ghafourian, “Predicting volume of distribution with decision tree-based regression methods using predicted tissue:plasma partition coefficients,” *J Cheminform*, vol. 7, Feb. 2015, doi: 10.1186/s13321-015-0054-x.
[84] A. Palczewska, J. Palczewski, R. M. Robinson, and D. Neagu, “Interpreting random forest classification models using a feature contribution method,” *arXiv:1312.1121 [cs]*, Dec. 2013.
[85] V. L. Berardi and G. P. Zhang, “An empirical investigation of bias and variance in time series forecasting: modeling considerations and error evaluation,” *IEEE Transactions on Neural Networks*, vol. 14, no. 3, pp. 668–679, May 2003, doi: 10.1109/TNN.2003.810601.
[86] H. Liang, X. Sun, Y. Sun, and Y. Gao, “Text feature extraction based on deep learning: a review,” *EURASIP J Wirel Commun Netw*, vol. 2017, no. 1, 2017, doi: 10.1186/s13638-017-0993-1.
[87] G. Louppe, “Understanding Random Forests: From Theory to Practice,” *arXiv:1407.7502 [stat]*, Jun. 2015.
[88] T. Hengl, M. Nussbaum, M. N. Wright, G. B. M. Heuvelink, and B. Gräler, “Random forest as a generic framework for predictive modeling of spatial and spatio-temporal variables,” *PeerJ*, vol. 6, Aug. 2018, doi: 10.7717/peerj.5518.
[89] E. Scornet, G. Biau, and J.-P. Vert, “Consistency of random forests,” *Ann. Statist.*, vol. 43, no. 4, pp. 1716–1741, Aug. 2015, doi: 10.1214/15-AOS1321.
[90] G. Biau, L. Devroye, and G. Lugosi, “Consistency of Random Forests and Other Averaging Classifiers,” *J. Mach. Learn. Res.*, vol. 9, pp. 2015–2033, 2008, doi: 10.1145/1390681.1442799.
[91] E. Scornet, “On the asymptotics of random forests,” *Journal of Multivariate Analysis*, vol. 146, pp. 72–83, Apr. 2016, doi: 10.1016/j.jmva.2015.06.009.
[92] R. Genuer, “Variance reduction in purely random forests,” *Journal of Nonparametric Statistics*, vol. 24, no. 3, pp. 543–562, Sep. 2012, doi: 10.1080/10485252.2012.677843.

[93] A. Ziegler and I. R. König, “Mining data with random forests: current options for real-world applications,” *WIREs Data Mining and Knowledge Discovery*, vol. 4, no. 1, pp. 55–63, 2014, doi: 10.1002/widm.1114.
[94] U. Grömping, “Variable importance in regression models,” *WIREs Computational Statistics*, vol. 7, no. 2, pp. 137–152, 2015, doi: 10.1002/wics.1346.
[95] M. Sakaguchi, H. Ogawa, N. Shimizu, H. Kanehisa, T. Yanai, and Y. Kawakami, “Gender differences in hip and ankle joint kinematics on knee abduction during running,” *Eur J Sport Sci*, vol. 14 Suppl 1, pp. S302-309, 2014, doi: 10.1080/17461391.2012.693953.
[96] H. K. Ramakrishnan and M. P. Kadaba, “On the estimation of joint kinematics during gait,” *Journal of Biomechanics*, vol. 24, no. 10, pp. 969–977, Jan. 1991, doi: 10.1016/0021-9290(91)90175-M.
[97] M. P. Kadaba, H. K. Ramakrishnan, M. E. Wootten, J. Gainey, G. Gorton, and G. V. Cochran, “Repeatability of kinematic, kinetic, and electromyographic data in normal adult gait,” *J. Orthop. Res.*, vol. 7, no. 6, pp. 849–860, 1989, doi: 10.1002/jor.1100070611.
[98] J. Nilsson and A. Thorstensson, “Ground reaction forces at different speeds of human walking and running,” *Acta Physiologica Scandinavica*, vol. 136, no. 2, pp. 217–227, 1989, doi: 10.1111/j.1748-1716.1989.tb08655.x.
[99] R. N. van Gent, D. Siem, M. van Middelkoop, A. G. van Os, S. M. A. Bierma-Zeinstra, and B. W. Koes, “Incidence and determinants of lower extremity running injuries in long distance runners: a systematic review,” *Br J Sports Med*, vol. 41, no. 8, pp. 469–480; discussion 480, Aug. 2007, doi: 10.1136/bjsm.2006.033548.
[100] Y. Adesida, E. Papi, and A. H. McGregor, “Exploring the Role of Wearable Technology in Sport Kinematics and Kinetics: A Systematic Review,” *Sensors*, vol. 19, no. 7, p. 1597, Jan. 2019, doi: 10.3390/s19071597.

Appendix A.

Senor's Raw Data Acquisition: LDC1614 register values

Table A.1. LDC1614 register values for reading the sensors.

Name	Address (Hex)	Value (Hex)
SETTLECNT_0	0x10	0x000A
SETTLECNT_1	0x11	0x000A
SETTLECNT_2	0x12	0x000A
SETTLECNT_3	0x13	0x000A
CLOCKDVDRS_0	0x14	0x1002
CLOCKDVDRS_1	0x15	0x1002
CLOCKDVDRS_2	0x16	0x1002
CLOCKDVDRS_3	0x17	0x1002
ERRORCONFIG	0x19	0x0000
MUXCONFIG	0x1B	0xC20D
DRVCURRENT_0	0x1E	0xF000
DRVCURRENT_1	0x1F	0xF000
DRVCURRENT_2	0x20	0xF000
DRVCURRENT_3	0x21	0xF000
CONFIG	0x1A	0x1601

Appendix B.

Senor Testing: Frequency test

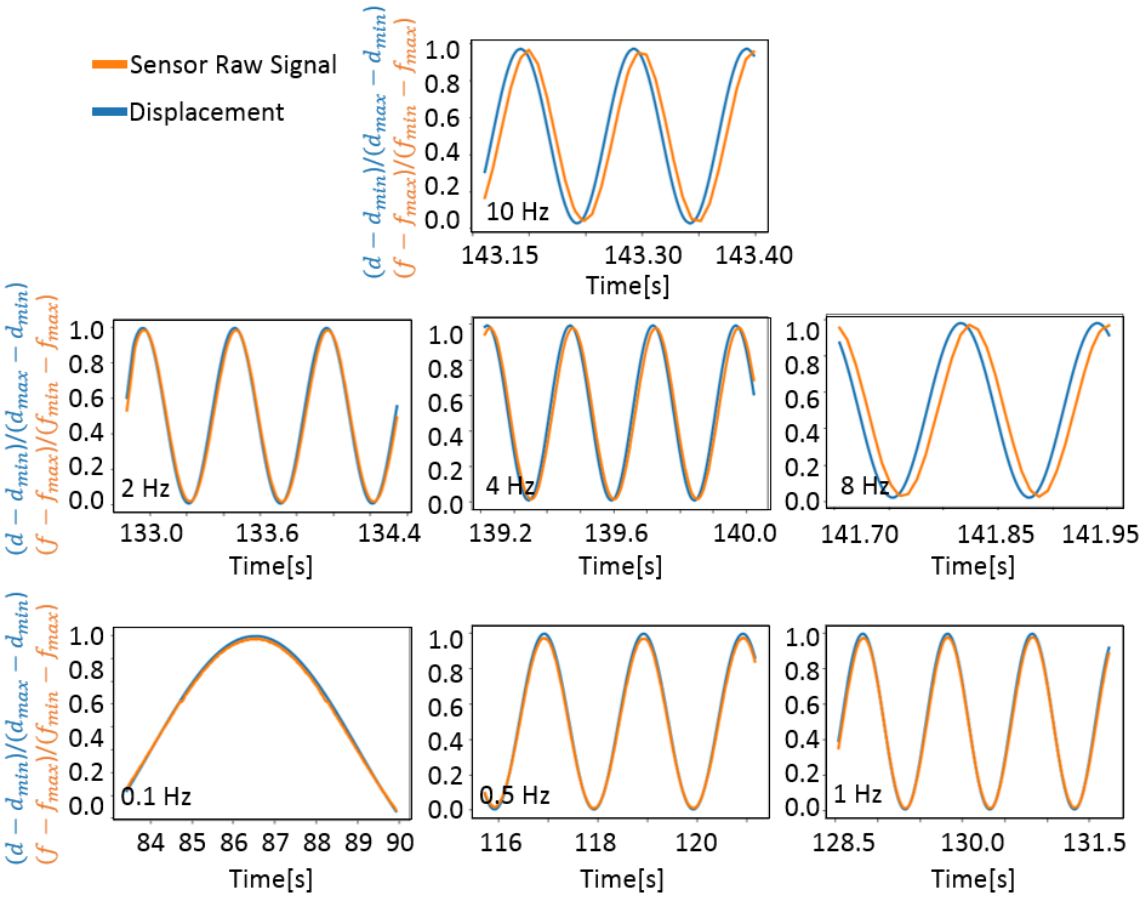

Figure B.1. Sensor raw signal and displacement results normalized in different frequency during frequency test A.

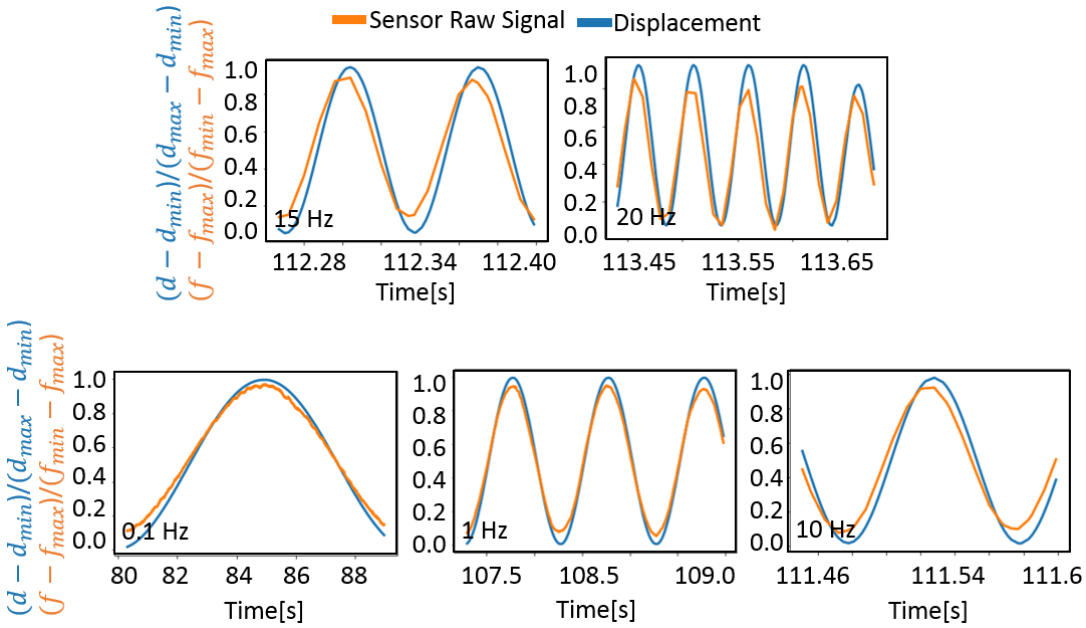

Figure B.2. Sensor raw signal and displacement results normalized in different frequency during frequency test B.

Appendix C.

Cohort Application Test Results

Table C.1. Performance results of the algorithm in the estimation of three angles in sagittal (ψ), frontal (θ) and transverse (ϕ) planes, among all participants, in 10-fold cross validation.

	Flex-Exte			Abd-Add			Rot		
ID	R^2	RMSE (deg)	NRMSE (%)	R^2	RMSE (deg)	NRMSE (%)	R^2	RMSE (deg)	NRMSE (%)
0	0.98	1.25	3.60	0.95	0.93	5.60	0.70	1.03	8.90
1	0.99	1.30	2.80	0.97	0.79	4.80	0.91	0.95	5.50
2	0.99	1.64	2.90	0.93	0.95	5.10	0.90	1.01	6.00
3	0.98	1.67	3.90	0.97	1.22	4.20	0.83	0.96	7.80
4	0.98	1.86	3.40	0.95	0.96	4.70	0.79	1.07	7.70
5	0.98	1.87	3.30	0.87	1.50	7.20	0.61	1.17	9.90
6	0.98	1.19	3.50	0.95	0.87	5.20	0.81	0.99	7.30
7	0.97	2.31	4.80	0.84	1.09	7.10	0.81	1.58	7.50
8	0.99	1.44	3.20	0.95	0.99	4.50	0.69	1.05	6.90
9	0.99	1.51	2.80	0.95	1.43	4.70	0.85	1.71	7.20
10	0.98	1.74	3.40	0.96	1.02	4.90	0.89	1.13	6.30
11	0.99	1.83	3.90	0.93	1.17	5.70	0.80	1.16	7.50

Table C.2. Performance results of the algorithm in the estimation of three angles in sagittal (ψ), frontal (θ) and transverse (ϕ) planes, among all participants, in 10-split forward chaining with 40 features.

	Flex-Exte			Abd-Add			Rot		
ID	R^2	RMSE (deg)	NRMSE (%)	R^2	RMSE (deg)	NRMSE (%)	R^2	RMSE (deg)	NRMSE (%)
0	0.94	2.07	6.00	0.89	1.27	7.70	0.56	1.29	10.10
1	0.99	1.68	3.60	0.95	0.95	5.70	0.88	1.10	6.30
2	0.98	2.19	3.90	0.90	1.13	6.20	0.88	1.10	6.80
3	0.98	1.89	4.40	0.96	1.23	4.80	0.88	1.03	6.30
4	0.98	2.29	4.20	0.95	0.80	5.50	0.88	1.27	6.80
5	0.97	2.46	4.40	0.74	1.97	9.90	0.52	1.28	10.80
6	0.98	1.48	4.30	0.93	1.06	6.00	0.76	1.10	8.10
7	0.96	2.51	5.20	0.81	1.21	7.80	0.77	1.74	8.10
8	0.97	2.24	4.90	0.92	1.34	6.00	0.53	1.28	8.50
9	0.98	2.17	4.00	0.92	1.82	5.80	0.79	2.03	8.30
10	0.97	2.42	4.60	0.91	1.45	6.60	0.84	1.39	7.60
11	0.97	2.06	4.50	0.91	1.32	6.30	0.77	1.27	8.30

Table C.3. Performance results of the algorithm in the estimation of three angles in sagittal (ψ), frontal (θ) and transverse (ϕ) planes, among all participants, in 10-split forward chaining with 720 features.

	Flex-Exte			Abd-Add			Rot		
ID	R^2	RMSE (deg)	NRMSE (%)	R^2	RMSE (deg)	NRMSE (%)	R^2	RMSE (deg)	NRMSE (%)
0	0.95	1.88	5.46	0.91	1.20	7.03	0.61	1.22	9.78
1	0.99	1.53	3.26	0.96	0.81	4.87	0.91	0.99	5.66
2	0.98	1.47	3.65	0.91	0.83	6.50	0.86	0.84	6.97
3	0.98	1.83	4.28	0.96	1.25	4.90	0.89	0.99	5.99
4	0.98	2.05	3.74	0.96	0.78	5.32	0.89	1.21	6.48
5	0.98	2.16	3.82	0.81	1.70	8.49	0.56	1.22	10.28
6	0.98	1.36	3.93	0.94	0.98	5.57	0.80	1.02	7.53
7	0.97	2.40	4.69	0.83	1.16	7.35	0.79	1.65	7.50
8	0.98	1.88	4.09	0.94	1.21	5.34	0.59	1.19	7.87
9	0.98	1.72	3.19	0.93	1.65	5.32	0.83	1.82	7.60
10	0.98	1.80	3.47	0.95	1.09	5.12	0.88	1.19	6.55
11	0.97	1.99	4.32	0.91	1.26	6.05	0.78	1.23	7.98